JGR Planets

RESEARCH ARTICLE
10.1029/2023JE007956

Key Points:

- Tidal, weather, and intra-seasonal eddies respond differently to dust forcing
- Eddy response depends on the location and season of dust forcing
- Positive and negative feedback between dust forcing and eddies may influence storm episode life cycles

Supporting Information:

Supporting Information may be found in the online version of this article.

Correspondence to:
H. Wang,
hwang@cfa.harvard.edu

Citation:
Wang, H., Toigo, A. D., & Richardson, M. I. (2023). Simulated atmospheric response to large-scale dust forcing and implications for Martian dust storm growth. *Journal of Geophysical Research: Planets*, *128*, e2023JE007956. https://doi.org/10.1029/2023JE007956

Received 20 JUN 2023
Accepted 18 SEP 2023

Author Contributions:
Conceptualization: Huiqun Wang, Anthony D. Toigo, Mark I. Richardson
Data curation: Huiqun Wang
Formal analysis: Huiqun Wang
Funding acquisition: Huiqun Wang, Anthony D. Toigo, Mark I. Richardson
Investigation: Huiqun Wang, Anthony D. Toigo, Mark I. Richardson
Methodology: Huiqun Wang, Anthony D. Toigo, Mark I. Richardson
Software: Huiqun Wang, Anthony D. Toigo, Mark I. Richardson
Supervision: Huiqun Wang
Visualization: Huiqun Wang
Writing – original draft: Huiqun Wang
Writing – review & editing: Huiqun Wang, Anthony D. Toigo, Mark I. Richardson

Simulated Atmospheric Response to Large-Scale Dust Forcing and Implications for Martian Dust Storm Growth

Huiqun Wang[1], Anthony D. Toigo[2], and Mark I. Richardson[3]

[1]Center for Astrophysics|Harvard-Smithsonian, Cambridge, MA, USA, [2]John Hopkins University Applied Physics Laboratory, Laurel, MD, USA, [3]Aeolis Research, Chandler, AZ, USA

Abstract The response of tidal, "weather," and intra-seasonal transient eddies in a global numerical model to dust imposed in different latitudinal bands and seasons has been examined in order to investigate the impact of regional scale dust storm episodes on large-scale circulation and hence on further dust storm development. The eddy kinetic energy and surface friction speed for each eddy group were derived using wavelet analysis from multi-year simulations and statistical comparisons were made among the experiments. Results show that different eddy categories respond differently to dust storm forcing, and that the responses are dependent upon both modeled storm location and season. These responses can be cast in terms of potential positive and negative feedbacks on large-scale dust storm development and have implications for the cascade of dust storms through different scales and circulation components. The model results suggest positive feedback between northern high latitude dust forcing and weather transients in the same latitudes in Quartober ($L_s = 185°–245°$), which weakens or disappears in Sixtober ($L_s = 295°–360°$). The results also suggest positive feedback between dust heating in the tropics/subtropics and tidal eddies, which may enhance the southward transport of "flushing" storms. However, southern high latitude dust forcing suppresses northern weather transients in both pseudo-season sextons, suggesting negative feedback which may terminate northern frontal/flushing dust storm sequences and hence weaken further development of a dust storm episode through this mechanism.

Plain Language Summary A global Martian atmosphere model is employed to investigate how large dust storm episodes change the atmospheric circulation and how these changes may affect the development of Martian dust storms. Results show that different circulation components—specifically, eddies with oscillation periods of shorter than approximately one sol (where a sol is one Mars day), several sols, and a dozen or more sols—respond differently to imposed dust storms, and that the responses depend upon both the modeled storm location and season. These responses suggest both positive and negative feedbacks for dust storm development. Large dust storm episodes in northern fall and winter often originate from the northern high latitudes where feedback is positive and would likely aid further storm growth. For the late stages of these episodes when dust resides mostly in the southern mid- or high latitudes, the feedback becomes negative and may help end further storm development. This study improves our understanding of the cascade of dust storms across scales, with different stages involving different mechanisms and different circulation components.

1. Introduction

Dust storms are important for the Martian climate system and can sometimes lead to dramatic changes in atmospheric opacity, thermal structure, and circulation (Kahre et al., 2017). Spacecraft observations have led to a relatively long record of dust storm climatology, and a wide range of scales for dust storms have been noted (e.g., Battalio & Wang, 2021; Cantor, 2007; Giuranna et al., 2021; Martin & Zurek, 1993; Montabone et al., 2015, 2020; Smith, 2008, 2019; Wang & Richardson, 2015). The occurrence and nature of dust storms has long been known to be non-uniform over the annual cycle. Kass et al. (2016) designated three main types ("A", "B," "C") of storms associated with three seasonal windows (time intervals) based on temperature observations, and these generally corresponded to dust storms observed in images (Wang & Richardson, 2015). Recently, Wang, Saidel, et al. (2023) proposed a hierarchical terminology for dust storm development and a sexton terminology to characterize the annual cycle in terms of dust storm types and other major features of the Martian climate. The hierarchical system designates significant dust events as dust storm episodes, where a dust storm episode is composed of dust storm sequences and a dust storm sequence is composed of dust storm members. The annual cycle consists of 6 pseudo-seasons or sextons—Unober, Duober, Triober, Quartober, Quintober, and Sixtober (or Sextober), with Quartober ($L_s = 185°–245°$) and Sixtober ($L_s = 295°–360°$) hosting most of the large dust storm episodes (Quartober corresponds approximately to the "A" and Sixtober to the "C" dust storm periods defined by Kass et al. (2016)). Large episodes typically last a few weeks and involve dust storm sequences from multiple origination regions.

An important question is how the Martian atmosphere both responds to and causes dust storms. Many studies have investigated the relationships between dust storms and the zonal mean circulation, thermal tides, and stationary or traveling waves using free running GCMs or data assimilation (e.g., Greybush, Gillespie, et al., 2019; Lee et al., 2018; Lewis & Barker, 2005; Mulholland et al., 2016; Streeter et al., 2021; Wilson, 2012a, 2012b; Wilson & Hamilton, 1996; Wilson et al., 2007). For example, Battalio and Wang (2020) analyzed the co-evolution of different types of transient eddies throughout the lifetimes of a set of observed dust storm episodes using a Mars data assimilation product. However, a comprehensive understanding of the process of eddy evolution during dust storm episodes is still lacking.

This paper performs general circulation model simulations of idealized dust storms to undertake a more systematic investigation of how eddies of different wave periods respond to dust storms of different sizes, locations, and seasons of occurrence. We focus on the kinetic energy and surface frictional velocity associated with the storm-associated eddies. Motivated by the observation that large dust storm episodes typically advance from the northern to the southern hemisphere in Quartober and Sixtober (northern fall and winter) (Battalio & Wang, 2021; Wang, Saidel, et al., 2023), we conducted idealized simulations for which dust is prescribed within different latitudinal bands. These simulations are designed to diagnose the dynamic effect of dust storm episodes that terminate at different latitudes or at different development stages during the journey of a large dust storm episode. To investigate the possibility of a seasonal dependence in the response, we conducted simulations during both Quartober and Sixtober.

2. Model

2.1. MarsWRF Simulations

MarsWRF global simulations were performed for this investigation. MarsWRF (Richardson et al., 2007; Toigo et al., 2012) is a multi-scale numerical model for the Martian atmosphere developed from the National Center for Atmospheric Research terrestrial Weather Research and Forecasting model (Powers et al., 2017). It is equipped with a set of well-tested parameterizations for radiative transfer, surface and subsurface heat balance, planetary boundary layer turbulence, cycles of CO_2 and H_2O, cycles of (prescribed or interactive) dust, and a two-moment, dynamically and microphysically interactive treatment of dust and ice interactions (Lee et al., 2018; Mischna et al., 2012; Newman et al., 2019; Toigo et al., 2012). To focus on the effect of dust in certain locations and time periods, we employ prescribed dust scenarios without any interaction with the water cycle or dust transport in this paper. We employ a resolution of 2° longitude × 2° latitude × 53 vertical level (with a model top at approximately 120 km) and archive the output every 2 model hours.

We perform MarsWRF simulations for a "no-storm" control run and a series of "dust storm" scenario runs with idealized dust enhancement. Each run spans about 10 Mars years and Year 1 is a "spin-up" year that is excluded from analysis. The no-storm dust scenario (Figure 1) is derived from the 9.3 μm absorption dust scenarios (3° × 3° resolution) for MY 24–34 (Montabone et al., 2015, 2020). To this end, we first find the second smallest column dust optical depth (τ) among all the years at each grid point on each sol (to avoid low bias effects of outliers), then apply a Fourier filter using the six lowest frequency terms for the annual time series at each grid point to retain the seasonal cycle, and finally perform an empirical orthogonal function analysis and reconstruct the dust field with six principal components which account for >99% of the variance. This procedure removes the opacity peaks associated with large dust storm episodes and high frequency noise, creating a smoothly varying dust field. Figure 1 shows that the no-storm dust scenario typically has the lowest global mean τ_{610} (τ at 9.3 μm scaled to 610 Pa) among the years used (or very close to it), as intended. The dust scenario has a maximum zonal mean τ_{610} of ~0.28 at 1.5°S and $L_S = 246°$, with a secondary maximum of ~0.20 at 4.5°S and $L_S = 332°$. The dust scenario is interpolated to the model grid and the exact seasonal date of each model radiation time step during the simulation, and then scaled to the local surface pressure.

For the dust storm scenario runs, we superimpose a column dust opacity enhancement ($\Delta\tau_{610}$) over the no-storm scenario (τ_{610}) at certain locations and for certain time (L_S) periods. The vertical dust distribution follows the MGS dust scenario (Lewis et al., 1999). To mimic the effect of dust at different latitudes during the progression

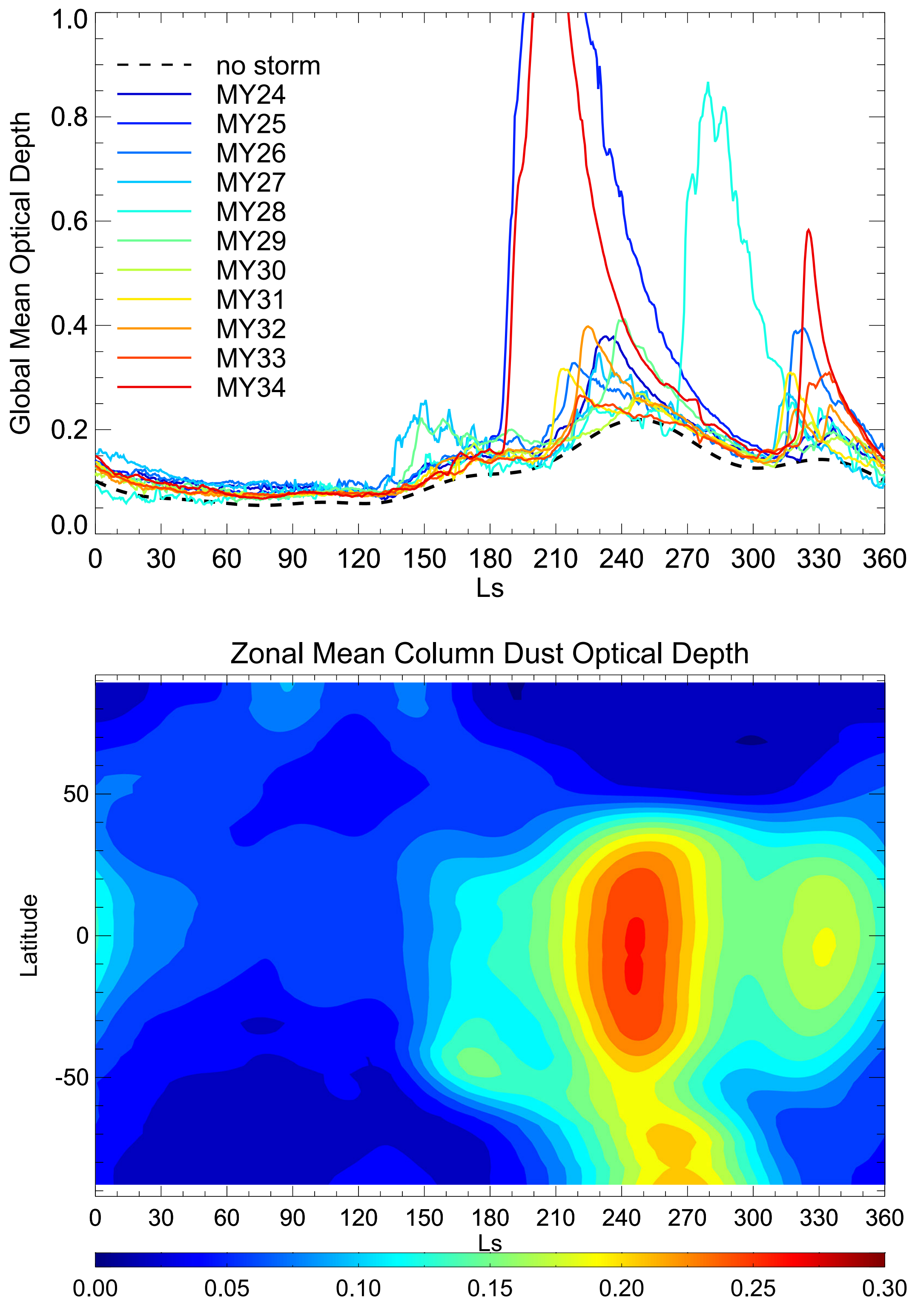

Figure 1. The "no-storm" dust scenario. (Top) Global mean dust optical depth as a function of L_S. The black dashed line represents the no-storm scenario, and other lines correspond to the Montabone et al. (2015, 2020) dust scenarios for MY 24–34. (Bottom) Latitude versus L_S distribution of zonal-mean dust optical depth for the no-storm scenario. The dust optical depths shown here refer to 9.3 µm absorption opacity normalized to a 610 Pa surface (τ_{610}).

Table 1
Dust Enhancements ($\Delta\tau_{610}$ at 9.3 μm) Prescribed in MarsWRF Dust Storm Simulations for Different Latitudinal Bands and L_S Ranges

	Lat				
L_s	75°S–45°S	45°S–15°S	15°S–15°N	15°N–45°N	45°N–75°N
200°–230° (in Quartober)	1.732	1.0	0.866	1.0	1.732
300°–330° (in Sextober)	1.732	1.0	0.866	1.0	1.732

of large dust storm episodes, we added dust within different latitudinal bands from the northern high latitudes to the southern high latitudes. As the most active sextons for dust storm episodes are observed to be Quartober and Sixtober (corresponding to the Kass et al. (2016) "A" and "C" storms), we have chosen to impose the additional dust within the $L_S = 200°–230°$ and $L_S = 300°–330°$ periods. To make a smoother temporal transition, and avoid numerical instabilities from imposed step functions, we also ramp up and down the additional dust over a 4° of L_S period outside each end of the 30° of L_s periods, for a total period of 38° of L_S. Although the duration of dust forcing used in these experiments is longer than that of typical dust storm episodes (Wang, Saidel, et al., 2023), this duration allows enough time to have elapsed to diagnose the circulation in a well-adjusted state for all relevant eddy periods examined in this paper. This duration is also motivated by a previous study demonstrating that significant circulation changes occur only when a dust storm is large enough and persists long enough (Toigo et al., 2018).

Table 1 lists the suite of dust storm runs conducted in this study. The amplitudes of the additionally imposed $\Delta\tau_{610}$ vary between 0.866 and 1.732 depending on the cosine of the central latitude of each band to roughly counteract the effect of the change in the surface area where dust is added. Locally, these are enhancement factors of about 3–6 over the maximum τ_{610} of the no-storm reference scenario. On a global average, the dust storm runs have τ_{610} peaks of 0.42 for Quartober and 0.37 for Sixtober (Figure S1 in Supporting Information S1), which are comparable to the observed large regional dust storm episodes.

2.2. Reanalysis Products

The OpenMARS (Version 1) (Holmes et al., 2020) and EMARS (Greybush, Kalnay, et al., 2019) reanalysis products are briefly used to test the analysis method and compare it with the MarsWRF simulations. These products were generated through assimilation of temperature and dust opacity data derived from thermal infrared observations into the underlying GCMs. OpenMARS is available in 2-hourly intervals at 5° latitude × 5° longitude resolution with 36 vertical layers. EMARS is available with hourly output at 5° × 6° resolution with 28 vertical layers. We note, however, that when the data necessary for these assimilation systems are scarce or missing, there can be spurious discontinuities in the reanalysis time series (Battalio, 2022).

3. Analysis Method

We perform wavelet analyses on the OpenMARS, EMARS, and MarsWRF time series to decompose the relevant meteorological variables into eddies with various oscillation wave periods (P). Wavelet decomposition and analysis are especially suitable for analyzing long complex non-stationary time series (Torrence & Compo, 1998) (e.g., the temperature and wind fields on Mars), and the sixth order Morlet wavelet function with 8 scales per octave is used in this paper. The analyses were performed using a 60-sol running window, typically every 10 sols. The analysis window length is chosen to capture a range of eddies from sub-diurnal to sub-seasonal time scales, while keeping the computational resources required at a reasonable level.

Figure 2 shows the analysis results for the OpenMARS temperature field on the $\sigma = 0.14$ ($z \sim 21$ km) vertical model level at representative latitudes (52.5°N, 2.5°S, and 52.5°S) for MY 24 and 26. This model level is chosen as it highlights well the differences in the eddy groups, as well as containing an abundance of observational data (e.g., as compared to levels nearer the surface). The color-filled contours in Figure 2 show the square root of the zonal mean of the scaled wavelet power (where scaled wavelet power = wavelet power/wavelet scale, and the square root is taken so that all panels can be similarly compared). The eddy power is shown as a function of L_S and equivalent Fourier wave period (P). The low latitudes are dominated by thermal tides, mostly with diurnal and

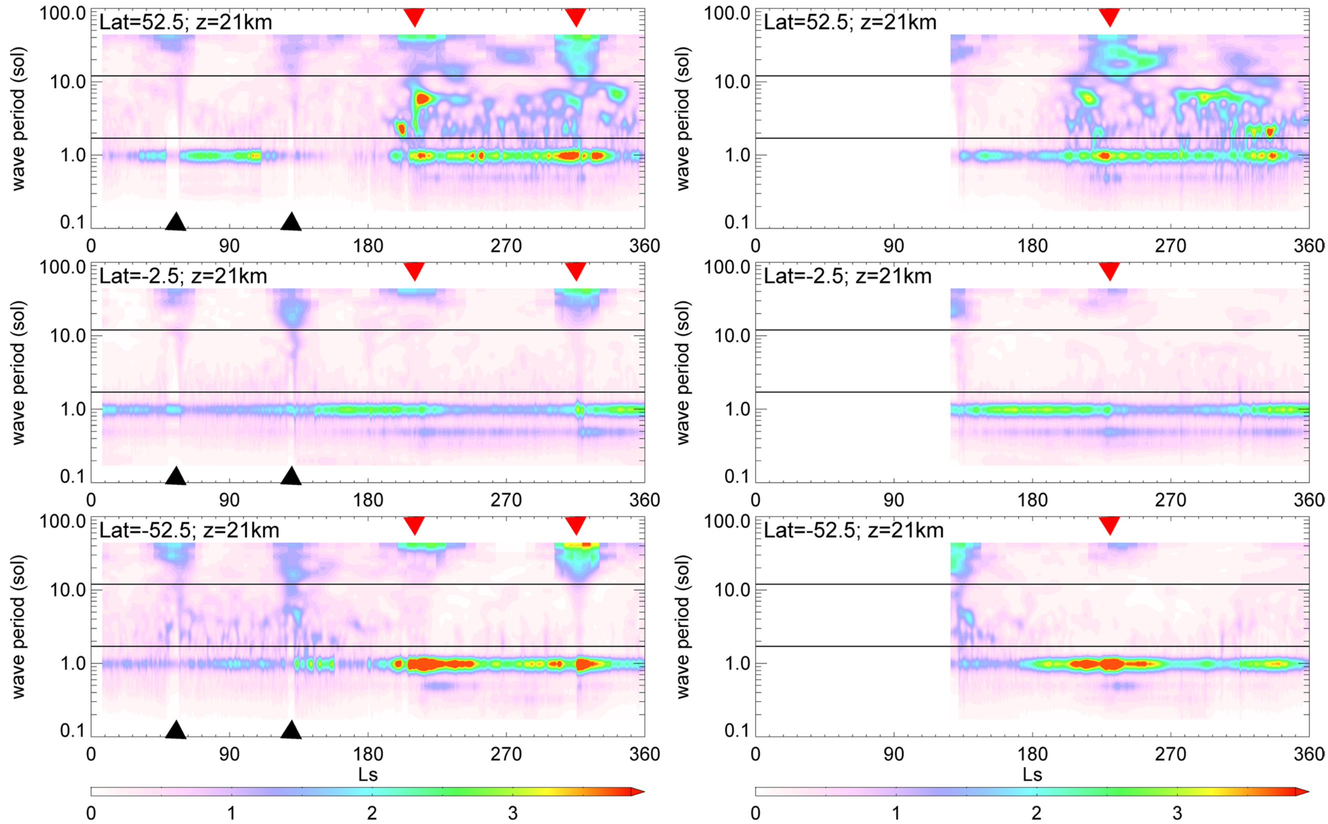

Figure 2. The spectral distribution of eddies in the temperature fields from the OpenMARS reanalysis at $z \sim 21$ km and (top row) 52.5°N, (middle row) 2.5°S, and (bottom row) 52.5°S for (left column) MY 26 and (right column) MY 24. The square root of the zonal mean of wavelet-scaled power is contoured in colors as a function of L_S and equivalent Fourier wave period. The wave period axis is on a logarithmic scale. Black lines indicate the boundaries of the three eddy groups.

semi-diurnal wave periods. Within the latitudinal bands represented by 52.5°N/S, the amplitudes of other eddies in the winter hemisphere become comparable in strength to the thermo-tidal components. Eddies with $P > 1$ sol are enhanced during the fall and winter in the northern hemisphere, with an indication of a solstitial pause near the winter solstice (Lewis et al., 2016; Toigo & Waugh, 2022). A similar pattern is suggested in the southern hemisphere. The abrupt changes indicated by the black arrows in the left column (around $L_s = 60°$ and 135° in MY 26) were spurious signals in the reanalysis due to a temporary dropout in observational data. However, the changes indicated by the red arrows (around $L_s = 210°$ and $L_s = 315°$ in MY 26, and $L_s = 230°$ in MY 24) are associated with large dust storm episodes (Battalio & Wang, 2020; Wang, 2017).

Figure 2 suggests that eddies in the Martian atmosphere can be divided into three groups which correspond to the fast (sub-diurnal and diurnal, which we call "tidal" for simplicity, though it includes both true thermal tides and resolvable eddies of other origins), intermediate (a few sols, which we call "weather transient") and slow (order 10 sols or longer, which we call "intra-seasonal" or "sub-seasonal") variations, respectively. Many of the wave modes within each group were identified in orbital and surface observations (e.g., Banfield et al., 2000, 2004, 2020; Barnes, 1980; Battalio et al., 2022; Harri et al., 2014; Hinson & Wilson, 2021; Hinson et al., 2012; Kleinböhl et al., 2013; Wang, 2017; Zurek & Leovy, 1981). Guided by the spectral distribution in Figure 2, we define the 3 groups using $P < 1.7$ sols, $1.7 \leq P < 12$ sols, and $12 \leq P < 60$ sols (or $P \geq 12$ sols for brevity) and indicate them using horizontal lines in Figure 2. Similar groupings were used in other studies (Battalio, 2022; Battalio & Wang, 2020). Wavelet analysis clarifies the reasoning for the particular categorization used here.

The inverse wavelet transform is used to reconstruct the signal for each wavelet scale (or wave period), following Equation 11 of Torrence and Compo (1998). The signals within each eddy group (range of eddy periods) are summed. As an example, the top panel of Figure 3 shows the OpenMARS time series of temperature at $z \sim 21$ km and 62.5°N and 180°W. After removing the 60-sol running mean, we reconstruct the signals for the $P < 1.7$ sols and $1.7 \leq P < 12$ sols eddies using the corresponding scales. To mitigate aliasing for the slow (long period)

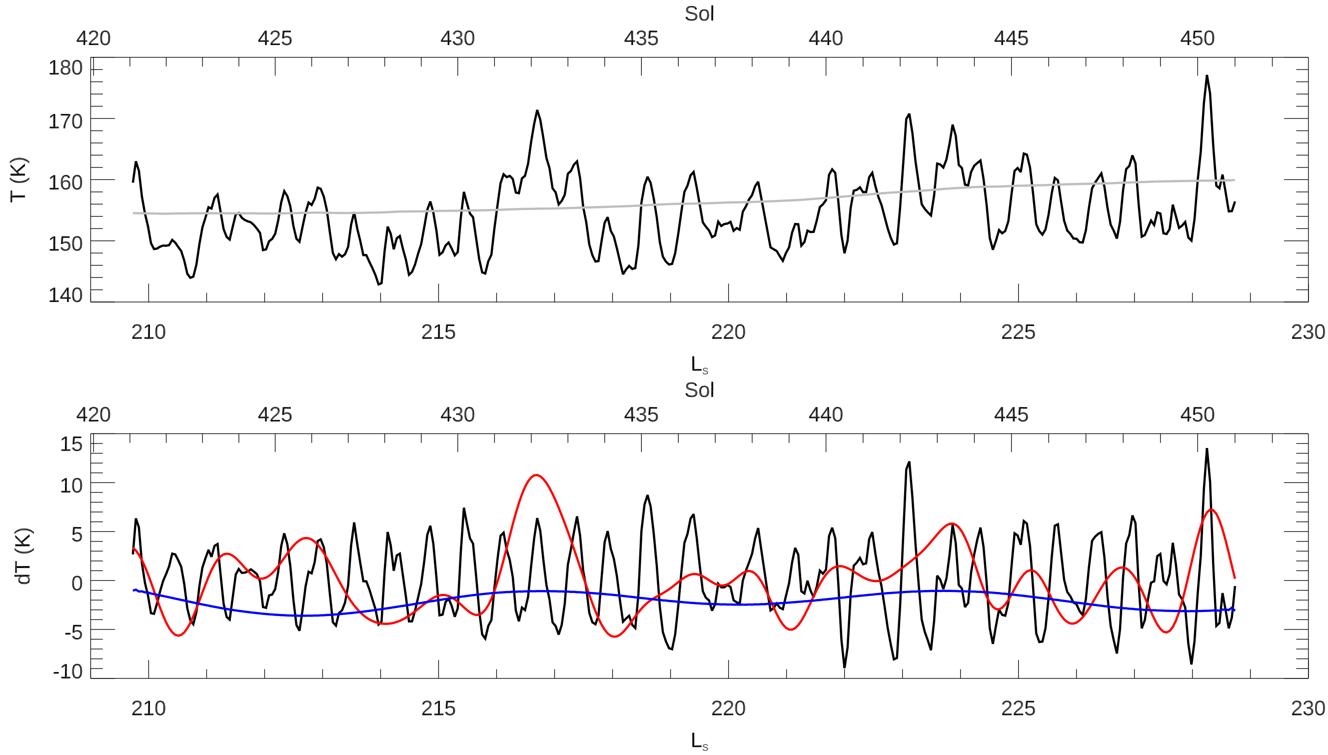

Figure 3. Time series of temperature at $z \sim 21$ km and 62.5°N 180°W from the OpenMARS reanalysis and its decompositions for MY 24 $L_S = 209.7°–228.7°$. Sol number is indicated in the upper axis. (Top) Original time series (black) and 60-sol running mean (gray). (Bottom) Time series for $P < 1.7$ sols (black), $1.7 \le P < 12$ sols (red), and $P \ge 12$ sols (blue).

waves associated with the finite length of the analysis window, we represent the $P \ge 12$ sols group using the residual signal, that is, the fast and intermediate groups subtracted from the detrended time series.

We perform the wavelet analysis on different variables of interest, such as zonal wind u, meridional wind v, and surface friction velocity $U*$. We derive the eddy kinetic energy per mass ($\text{EKE} = \left(u'^2 + v'^2\right)/2$, in units of J/kg = m^2/s^2) for each eddy group using the perturbation winds reconstructed from the wavelet analysis. To condense the information on how the global circulation varies among the experiments, we calculate the mass-weighted vertical average of EKE (i.e., $\overline{\text{EKE}}$, where the overbar denotes a mass-weighted vertical average) and global mass average of EKE (i.e., $\langle \text{EKE} \rangle$, where the angular brackets denote a mass-weighted global average) at each output time step. The mass-weighted vertical average uses density (ρ), or equivalently pressure (p), as a weight (*i.e.*, $\int \rho \bullet \text{EKE} dz / \int \rho dz = \int \text{EKE} dp / \int dp$, where z denotes height, and integration operates on all grid boxes of interest).

Figure 4 shows the EKE results derived for OpenMARS MY 26 and a MarsWRF simulation driven by the MY 26 dust scenario (Montabone et al., 2015). The bottom row shows the time series of the square root of the globally mass-averaged EKE (i.e., $\sqrt{\langle \text{EKE} \rangle}$, in units of m/s) for each eddy group as a different colored line. The square root is taken so that the range of the vertical axis can be more readily compared across all eddy groups. For reference, the global mean τ_{610} is plotted in gray and uses the right-hand axis for scale. The other three rows from upper to lower show the latitude versus L_S distributions of the square root of the zonal mean of the vertically mass averaged EKE (i.e., $\sqrt{\left[\overline{\text{EKE}}\right]}$, where the square brackets denote a zonal mean) for the intra-seasonal, weather transient, and tidal eddy groups, respectively. The comparison with EMARS in the same panel format is shown in Figure S2 in Supporting Information S1.

MarsWRF shows a general evolution of the EKE terms that is similar to both of the OpenMARS and EMARS results (neglecting the time periods with spurious signals in the reanalysis products). MarsWRF results often reside between the results derived from the two reanalyses. On the global scale, the tidal EKE is dominant among the 3 eddy groups. It is the strongest in the southern hemisphere in Quartober, Quintober, and Sixtober, especially

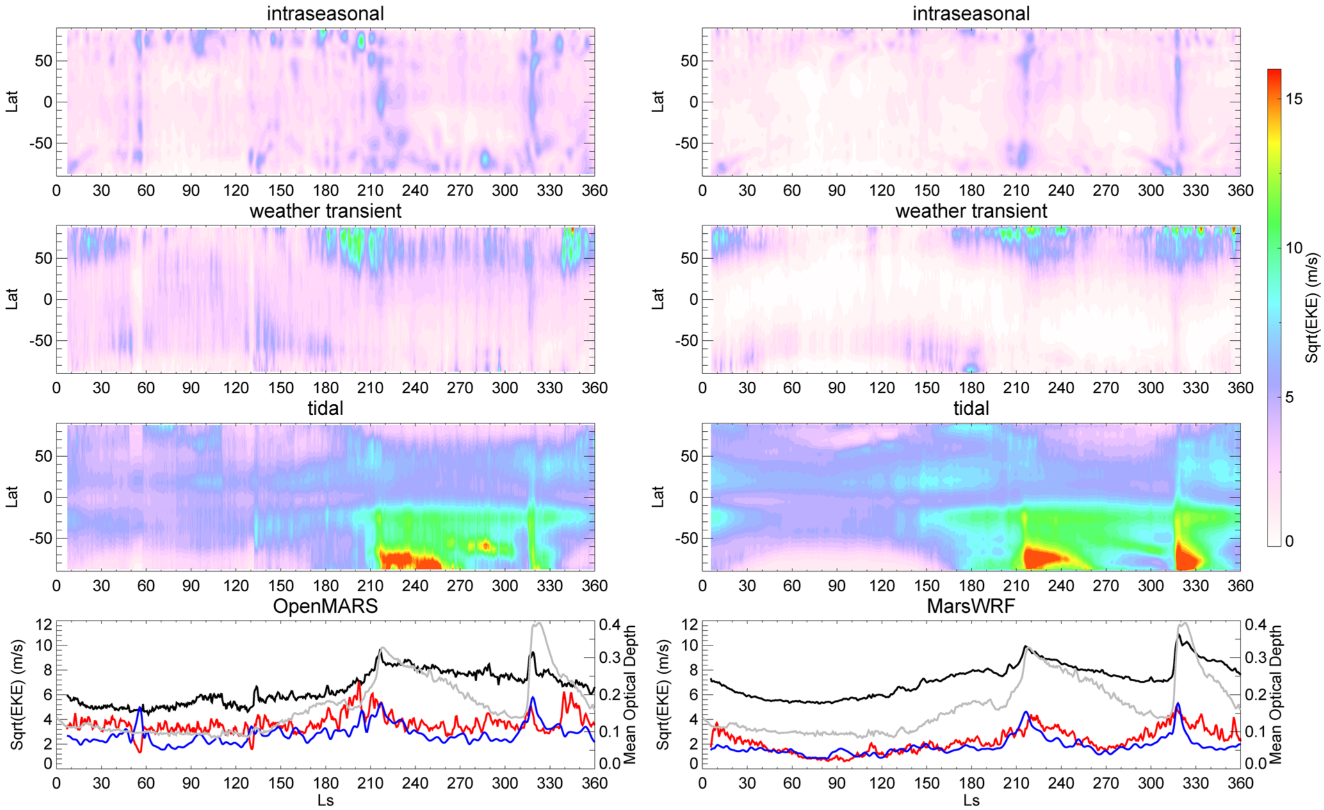

Figure 4. Color-filled contours show the L_S versus latitude distributions of the square root of the zonal mean of the vertically averaged EKE for eddies (i.e., $\sqrt{[\overline{\mathrm{EKE}}]}$) in the intra-seasonal ($P \geq 12$ sols, top row), weather transient ($1.7 \leq P < 12$ sols, second row), and tidal ($P < 1.7$ sols, third row) groups. Panels in the bottom row show the time series of the square root of the global average EKE (i.e., $\sqrt{\langle \mathrm{EKE} \rangle}$) for (black) tidal, (red) weather transient, and (blue) intra-seasonal eddies. For reference, gray lines show the global mean τ_{610} used in the models. Results are for MY 26, with OpenMARS on the left and MarsWRF on the right.

during large dust storm episodes. The intra-seasonal eddies are enhanced when big changes occur, such as a large dust storm episode, or in the case of the reanalyses, a jump in the amount of available data for assimilation. The weather transient eddies are most active at the northern mid-high latitudes in Quartober and Sixtober, with a suppression of EKE in Quintober that is related to the observed solstitial pause in eddy activity (Lewis et al., 2016; Toigo & Waugh, 2022).

4. Results

4.1. "No-Storm" Control Run

To establish a baseline for comparison, we investigate the annual cycle of $\sqrt{\langle \mathrm{EKE} \rangle}$ for the no-storm control run. Figures 5a–5c show the results for the $P < 1.7$ sols, $1.7 \leq P < 12$ sols, and $P \geq 12$ sols eddies, respectively. Note that the global average eddy kinetic energy, $\langle \mathrm{EKE} \rangle$, is dominated by the contributions from 75°S to 75°N (Figure S3 in Supporting Information S1), where the model results are not significantly affected by the numerical polar filtering. Two Mars years are arbitrarily chosen from the multi-year simulation and are plotted in different colors. Each eddy group closely follows a characteristic annual cycle from year to year. However, there are some differences between the years, even though the prescribed dust field repeats every Mars year. Weather transients exhibit the most interannual variability (Figure 5b) due to the chaotic nature of the dynamical system (Greybush et al., 2013; Newman et al., 2004). This implies that comparisons with other runs are best done in a statistical sense.

Thus, we derive the mean annual cycle and its standard deviation for each eddy group using 9 Mars years of 2-hourly outputs. To this end, we calculated the mean and standard deviation (σ) for all the output time steps within each 10° L_S bin (with a 5° L_S stride). Results are shown in Figure 5d, where the area within $\pm 1\sigma$ of the

10.1029/2023JE007956

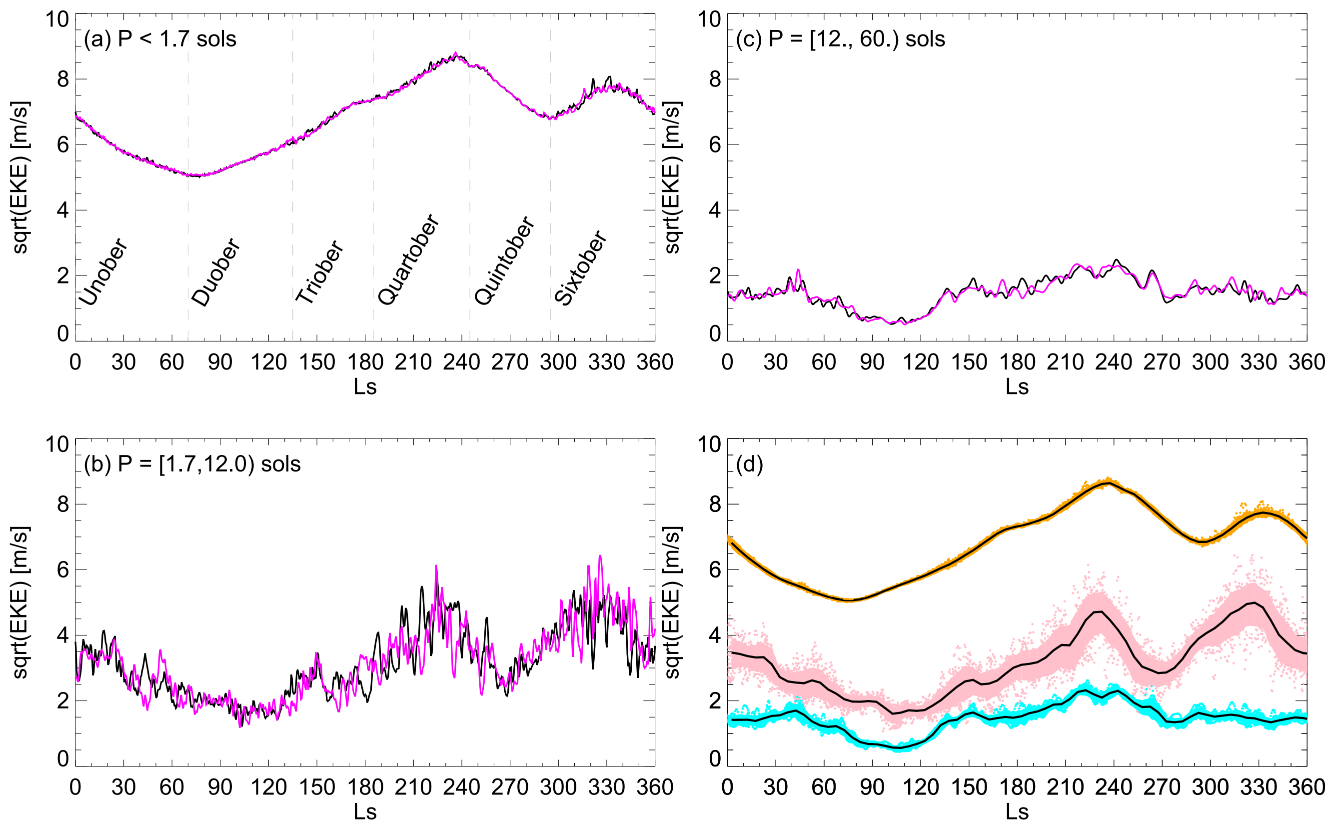

Figure 5. Eddy results for the MarsWRF "no-storm" control run. The sextons are indicated by vertical dashed lines in Panel (a). $\sqrt{\langle \mathrm{EKE} \rangle}$ (m/s) as a function of L_S for the (a) tidal $P < 1.7$ sols, (b) "weather" $1.7 \leq P < 12$ sols, and (c) intra-seasonal $P \geq 12$ sols groups for two arbitrary Mars years are shown in black and magenta, respectively. (d) Multi-year mean $\sqrt{\langle \mathrm{EKE} \rangle}$ (m/s) as a function of L_S for the (upper) $P < 1.7$ sols, (middle) $1.7 \leq P < 12$ sols, and (lower) $12 \leq P < 60$ sols eddies are shown in black lines. The color-shaded area around each line represents 1σ variation from the mean for the corresponding eddy group. The dots indicate outliers beyond 1σ.

mean for each eddy group is shaded, and the outliers are plotted as dots. In subsequent sections, we will use the shaded areas to make comparisons. It is worth noting that any linear temporal trend within each L_S bin is included during the calculation of the temporal standard deviation. For most cases studied in this paper, the trends are small; but, as will be shown later (Figure 6), the tidal group during the "ramping" time periods has a large temporal change that contributes strongly to the standard deviation and aliases as an apparent variation.

4.2. Quartober Results

The Quartober MarsWRF runs have additional dust imposed during the $L_S = 200°–230°$ period. The individual runs have dust prescribed within different 30°-wide latitudinal bands, where the bands in different runs are centered at different latitudes over the range from 75°S to 75°N (see Table 1).

4.2.1. Eddy Kinetic Energy

The $\sqrt{\langle \mathrm{EKE} \rangle}$ for the three eddy groups and for each Quartober run are plotted in hatching in Figures 6a–6e following the same method as that for Figure 5d. To facilitate comparison, the result for the no-storm control run (i.e., Figure 5d) is superposed in each panel. For each run, different eddy groups respond differently to the dust forcing. Across the runs, the effects vary significantly with the latitude of imposed dust.

The EKE of the tidal group is enhanced during the imposed dust storms, as expected from previous studies (e.g., Lewis & Barker, 2005; Wilson, 2012a, 2012b; Wilson & Hamilton, 1996). There is a very large dependence of the enhancement upon the dust storm latitude. The enhancement is the largest for the equatorially-centered 15°S–15°N run where the ⟨EKE⟩ increased by a factor of about 3.5 compared to the no-storm run. In this case, the sharp rise and fall near the edges of the forcing time period dominate the standard deviation and alias as apparent variations (see Section 4.1). The annual cycle of the tidal ⟨EKE⟩ is in fact highly repeatable. The ⟨EKE⟩

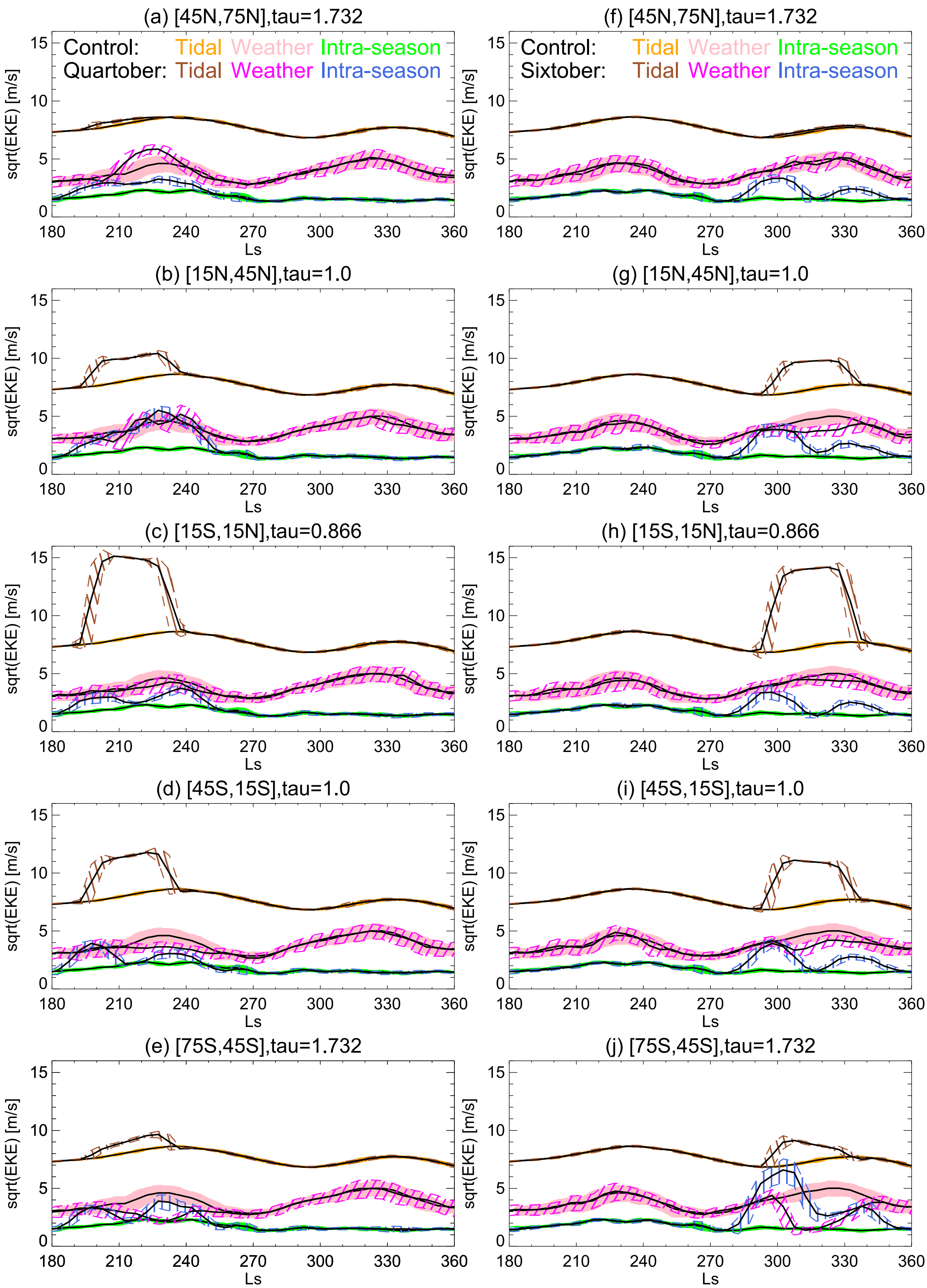

Figure 6. $\sqrt{\langle \mathrm{EKE} \rangle}$ (m/s) as a function of L_s for the (a–e) Quartober and (f–j) Sixtober runs. Dust is imposed in (a, f) 75°N–45°N, (b, g) 45°N–15°N, (c, h) 15°S–15°N, (d, i) 15°S–45°S, and (e, j) 45°S–75°S. Each panel is in the same format as Figure 5d, but the $P < 1.7$ sols tidal group is in brown hatching, the $1.7 \leq P < 12$ sols weather group in magenta hatching, and the $P \geq 12$ sols intra-seasonal group in blue hatching (outliers are omitted for clarity). For ease of comparison, the corresponding results for the control run are overplotted in shading in each panel, with the $P < 1.7$ sol group in brown, the $12 \leq P < 60$ sol group in pink, and the $P \geq 12$ sols group in green. Black lines indicate the corresponding multi-year means.

enhancement decreases as the forcing is placed at higher latitudes and decreases faster as the forcing is placed progressively closer to the northern pole than to the southern pole. The results suggest that the tidal ⟨EKE⟩ is most sensitive to the amount of dust increase at low latitudes. Furthermore, in the context of large dust episodes (Wang, Saidel, et al., 2023), following the early stage of a northern hemisphere flushing event, subsequent low-latitude dust lifting (if any) will likely excite the tidal group and mean flow more than it will the weather group.

The intra-seasonal group is enhanced with two peaks, one near $L_S = 200°$ and the other near $L_S = 230°$, corresponding to the times with the greatest time rate of change in dust opacity. The excitement of this eddy group probably reflects atmospheric adjustment to this change, involving the generation of slow waves propagating both eastward and westward (Banfield et al., 2004; Wang, 2017). The durations and relative amplitudes of the intra-seasonal signals vary among the runs. The runs with the southern hemisphere forcing have two well-separated peaks in time, while those with the northern hemisphere forcing appear to have a broad increase with hints of two local peaks. The strongest effect for intra-seasonal eddies was shown in the 15°N—45°N run.

The weather transient group ⟨EKE⟩ response changes from enhancement to suppression as the forcing changes from the northern high latitudes to the southern high latitudes, with the transition occurring for a forcing between the 15°N–45°N run and the 15°S–15°N run. The ⟨EKE⟩ for the 75°S–45°S run is only ∼20% that of the no-storm run, which is more than 1 standard deviation below the no-storm run mean during the imposed dust storm period. In comparison, the ⟨EKE⟩ for the 45°N–75°N run is ∼1.8 times that of the no-storm run, which is more than 1 standard deviation above the no-storm run mean during this time period.

The dependence of the weather transients on storm latitude suggests a positive-negative feedback sequence that can help explain the development history of large dust storm episodes. Observations show that a large dust storm episode usually initiates from many northern high latitude frontal dust storms associated with baroclinic eddies (Battalio & Wang, 2020; Hinson et al., 2012; Wang et al., 2005). Our simulations suggest that dust at this stage tends to enhance these eddies (which have wave periods in the weather transient group), resulting in more vigorous frontal dust storms and increasing their chance of becoming flushing dust storms (Hinson et al., 2012; Wang et al., 2003).

With the development of a dust storm episode, dust advances southward into the low northern latitudes as flushing dust storms (Wang, Saidel, et al., 2023). With this southward advancement, the positive feedback weakens, as a dust enhancement at lower latitudes no longer drives as large an enhancement of the weather transients. Instead, the dust forcing strengthens the tidal group. At this stage, the tidal group is probably more efficient at driving any low latitude dust activity than the weather group (Wilson, 2012a, 2012b).

After dust arrives in the southern hemisphere, the feedback becomes negative, that is, the northern high latitude weather transient eddies become suppressed, which tends to reduce the effectiveness of dust storm initiation and frontal/flushing dust storm growth in the northern hemisphere. The weakening of the northern hemisphere weather transients appears to result from the enhanced meridional circulation associated with dust heating in the southern hemisphere. The increased interhemispheric transport of heat tends to reduce the overall winter hemisphere baroclinicity. As will be discussed later, the weakened northern hemisphere weather eddies are also associated with weaker baroclinic energy conversion.

To further understand the changes described above, we compare the multi-year mean of the $\sqrt{\left[\overline{\mathrm{KE}_m}\right]}$ and $\sqrt{\left[\overline{\mathrm{EKE}}\right]}$ for the control run, the 75°S–45°S, and the 45°N–75°N Quartober run (Figure 7). Here, KE_m is the kinetic energy of the mean flow and is shown to provide context ($\mathrm{KE}_m = ½\left(U_m{}^2 + V_m{}^2\right)$, and U_m and V_m are the 60-sol running-mean wind components). The multi-year mean was calculated for each 10° L_s bin. Across all runs, the mean flow kinetic energy is generally strongest near the fall and winter polar cap edges, with a secondary maximum at low southern latitudes during southern spring and summer. The maximum near the north polar cap greatly weakens in the 75°S–45°S run and slightly strengthens in the 45°N–7°5N run during the dust forcing time period $L_S = 200°$–$230°$ (Figures 7a, 7e, and 7i).

The EKE of the intra-seasonal eddies is mainly seen near the polar caps during the growth and decay phases (Figure 7b). These eddies are strengthened near the beginning and end of the dust forcing period, although the location and magnitude of this strengthening can vary widely in latitude depending on the region of dust forcing. The 75°S–45°S run affects the high latitudes in both hemispheres, while the 45°N–75°N run mainly affects

10.1029/2023JE007956

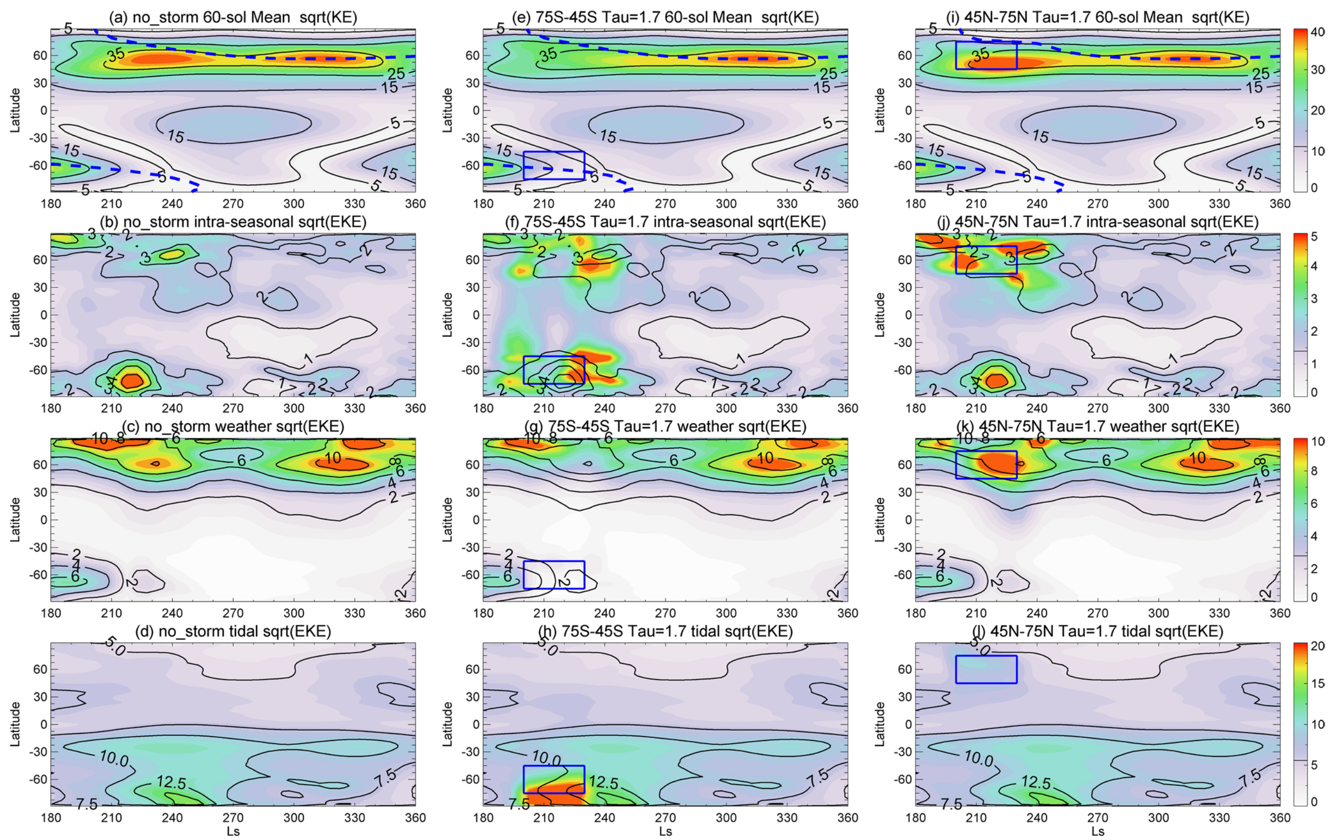

Figure 7. Color shading shows the latitude versus L_s distribution of (a, e, i) $\sqrt{[\mathrm{KE}_m]}$ (m/s) for the multi-year 60-sol running mean; and that of $\sqrt{[\mathrm{EKE}]}$ (m/s) for (b, f, j) $P \geq 12$ sols, (c, g, k) $1.7 \leq P < 12$ sols, and (d, h, l) $P < 1.7$ sols eddies. The columns correspond to specific simulation runs (a–d) control run, (e–h) 75°S–45°S Quartober run, and (i–l) 45°N–75°N Quartober run. Note the scaling changes for each row. For ease of comparison, the values from the control run are overplotted in black contours in each panel in the same row. Blue dashed lines in (a, e, i) denote the notional polar cap edges, defined for convenience by 100 kg/m^2 of the surface CO_2 ice field. Blue boxes in (e–l) indicate the time intervals and latitudes of imposed dust.

the northern hemisphere (Figures 7f and 7j). For the runs with dust forcing at lower latitudes, additional local maxima appear at low latitudes, with the largest effect seen in the 15°N–45°N Quartober run (Figures S4b, S4f, and S4j in Supporting Information S1).

Weather transient EKE is also generally concentrated near the polar caps (Figures 7c, 7g, and 7k). The eddies are stronger in the northern hemisphere and show solstitial pauses (Figure S4 in Supporting Information S1). We note that the eddies within 75°S–75°N dominate the global mass average ⟨EKE⟩ (Figure S3 in Supporting Information S1); thus, the eddy power adjacent to the pole (where the model polar filter may cause artificial changes in the EKE) is less important from a global-mean perspective than that in lower latitudes (<75°). The weather transient eddies near 60°N were greatly weakened in the 75°S–45°S run and significantly strengthened in the 45°N–75°N run. The 45°S–15°S and 15°S–15°N runs also show depressed transient eddies near 60°N, and the 15°N–45°N run shows some enhancement during the forcing time period (Figures S4c, S4g, and S4k in Supporting Information S1).

The EKE of the tidal eddies is generally strongest in the southern hemisphere during Quartober and Quintober (Figures 7d, 7h, and 7l). Strong enhancement during the period of dust storm imposition is seen at southern high latitudes for the 75°S–45°S run and a much milder enhancement at the northern mid- to high latitudes for the 45°N–75°N run. As the dust forcing is shifted to lower latitudes, so is the tidal eddy enhancement, with more enhancement when the forcing is in the southern hemisphere than in the northern hemisphere (Figures S4d, S4h, and S4l in Supporting Information S1). For the 45°S–15°S and 15°S–15°N runs, the latitudes apparently influenced by tidal eddy enhancement extend well beyond the latitudes with imposed dust, as would be expected from the global response of thermal tides (Wilson, 2012a, 2012b).

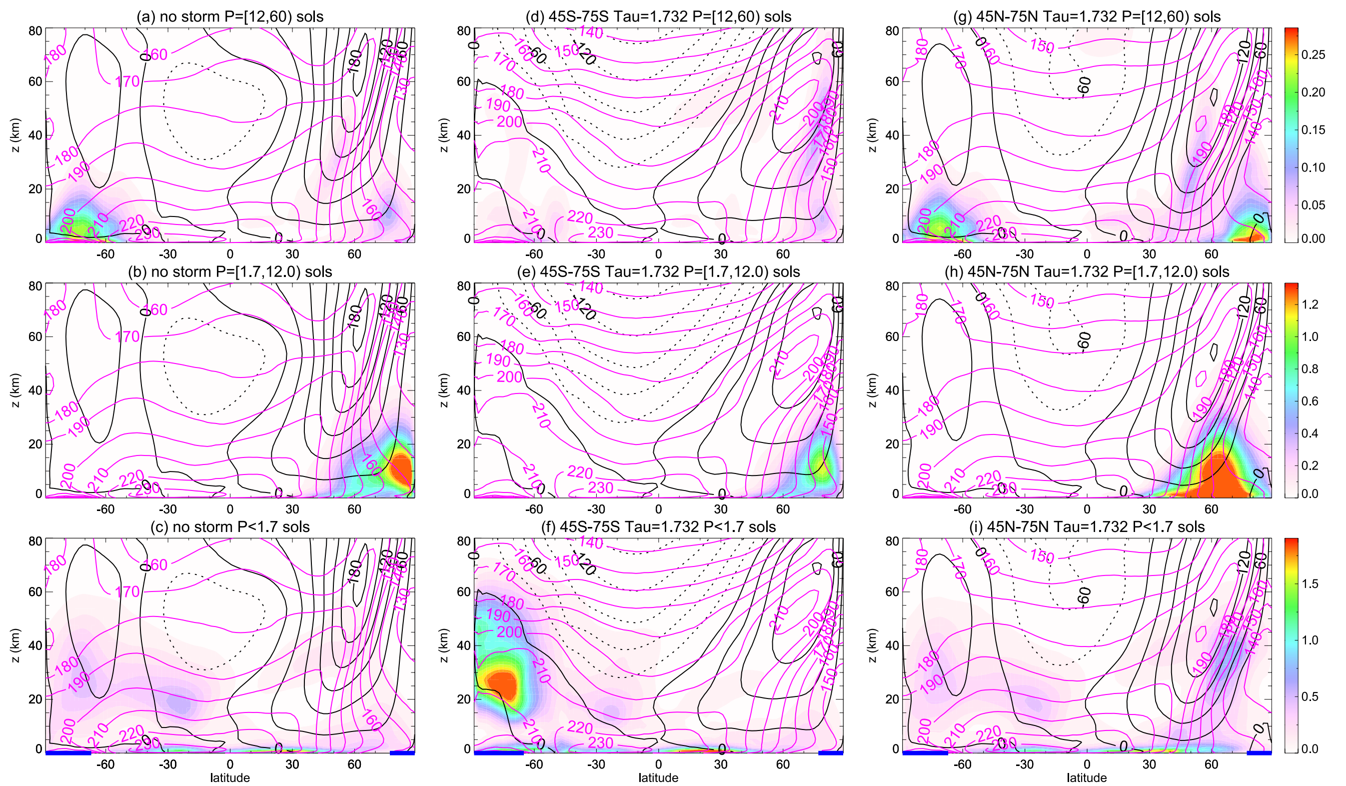

Figure 8. Zonal mean of the eddy kinetic energy density (J/m^3, color filled contours) for (a, d, g) $P \geq 12$ sols, (b, e, h) $1.7 \leq P < 12$ sols, and (c, f, i) $P < 1.7$ sols eddies as a function of latitude and pseudoheight $z = 10.8$ km • ln(610/p) (where p is in Pa) for $L_s = 210°–220°$ for the (a–c) no-storm run, (d–f) 75°S–45°S Quartober run, and (g–i) 45°N–75°N Quartober run. Note that the color bar for each eddy group (row) is on a different scale. The zonal mean of the 60-sol mean zonal wind U_m (m/s) and temperature T_m (K) centered on $L_s = 215°$ are overplotted in black and magenta, respectively. Thick blue lines in the bottom row panels indicate the latitudinal extent of the polar caps.

Figure 8 shows the zonal mean EKE density per volume [eke] (where eke = $\rho_m \cdot$ EKE in units of J/m^3 and ρ_m is the 60-sol running mean density at that location) for the three eddy groups for the no-storm run, 75°S–45°S Quartober run, and 45°N–75°N Quartober run. The results are derived by first averaging the eke at each location within the $L_S = 210°—220°$ period over all non-spinup Mars years of the runs and then averaging over all longitudes.

The zonal mean of the 60-sol mean zonal wind ([U_m]) and temperature ([T_m]) centered at $L_S = 215°$ are also shown in Figure 8 for reference. Within the bottom $z \sim 20$ km of the atmosphere in the northern mid-latitudes, the latitudinal temperature gradient of the 45°N–75°N run is larger than that of the control run, and consistent with the thermal wind balance, the vertical wind shear there is also larger. However, the maximum wind speed in the polar jet is larger in the control run, as the region of warmer air near the pole in the 45°N–75°N run decreases the latitudinal temperature gradient at higher altitudes, leading to an overall weaker jet. In the 75°S–45°S run, dust heating occurs in the summer hemisphere, the latitudinal temperature gradient below $z \sim 20$ km in the winter hemisphere is similar to or slightly weaker than that in the control run, but the increased cross-equatorial Hadley circulation results in warm air being transported nearer to the winter pole at higher altitudes, leading to a polar jet that is weaker than in the control run.

Figures 8b, 8e, and 8h show that the weather transient eke is strongest in the northern high latitudes below $z \sim 20$ km, poleward of the sharp latitudinal temperature gradient at the polar vortex edge. In the 45°N–75°N run, the eke is much stronger over a wider range of altitudes and latitudes, extending farther equatorward near the surface. On the contrary, for the 75°S–45°S run, the eddies are weaker but cover a similar latitude and altitude range as in the no-storm case. These results are further quantified by the baroclinic and barotropic energy conversion rates calculated using the Sheng and Derome (1991) formula. The zonal mean conversion rates (J m^{-3} s^{-1}) averaged over $L_S = 210°–220°$ of a Mars year are shown in Figure S5 in Supporting Information S1. For the 45°N–75°N run, strong baroclinic conversion from zonal mean flow to transient eddies is seen along the sharp temperature gradient in the northern mid-latitudes below $z \sim 20$ km; there is also a barotropic energy conversion from the eddies to the mean flow in this region, but its magnitude is only ∼20% of that of baroclinic conversion. The net result is a strong baroclinic production of transient eddy energy. In contrast, for the 75°S–45°S run, the baroclinic conversion is much weaker, while the barotropic conversion becomes relatively more significant, and thus the net result is barotropic dissipation of the transient eddies near the winter pole.

For the $P < 1.7$ sols tidal eddies, Figures 8c, 8f, and 8i show that the eke is greatly enhanced at the southern high latitudes between $z \sim 10$ and 50 km in the 45°S–75°S run. A similar enhancement is seen at high northern latitudes over the same vertical region in the 45°N–75°N run, but of much smaller magnitude (∼1/3 as strong). This difference is consistent with the southern hemisphere dust being much more strongly heated by the Sun than the northern hemisphere dust. Enhancements of tidal eke are also seen for the other Quartober runs (Figures S6c, S6f, and S6i in Supporting Information S1), where the latitudinal region of maximum enhancement shifts northward as the central latitude of the imposed dust storm shifts northward. For the 45°S–15°S and 15°S–15°N runs, there are significant additional increases in the tidal eke below $z \sim 5$ km at some latitudes.

For the $P \geq 12$ sols intra-seasonal eddies, the control run, 45°S–15°S, and 15°S–15°N Quartober run, all have eke largest in the region below $z \sim 15$ km over the south polar cap (Figure 8a; Figures S6a and S6d in Supporting Information S1). In the 45°N–75°N run, the near-surface region above the north polar cap becomes an additional region of strong eddy activity (Figure 8g). The 15°N–45°N run shows strong eddy activity in both regions, as well as near the equatorward edge of the winter polar jet axis below $z \sim 30$ km (Figure S6g in Supporting Information S1). There are no regions of large eke in the 75°S–45°S run (Figure 8d), consistent with the result in Figure 6e, which shows a local minimum in the intra-seasonal ⟨EKE⟩ near $L_s = 215°$. However, enhancements in eddy strength are seen toward both the beginning and end of the dust forcing period (not shown).

4.2.2. Surface Friction Velocity

The surface friction velocity (U^*) is directly related to dust lifting (Kahre et al., 2017; Newman & Richardson, 2015) and thus changes in U^* may yield insight into dynamical-dust lifting feedback. In Figure 9, we show how U^* differs between the control run, 75°S–45°S Quartober run, and 45°N–75°N Quartober run. We calculate the wavelet power of U^* associated with the intra-seasonal, weather transient, and tidal eddy groups following Equation 24 of Torrence and Compo (1998). The results are averaged in 10° L_s bins across Mars years for each run, and the square root of the zonal mean power is plotted in Figure 9. For context, the zonal mean of the 60-sol mean U^* (i.e., $[U_m^*]$) is also shown.

The intra-seasonal eddy power is the weakest among the three groups, with the maximum located in the polar regions. Mild enhancements are seen in the northern high latitudes near the beginning and end of the forcing period for the 45°N–75°N run. The power of the weather transient group is concentrated around the edges of both polar caps from the fall to spring, with a suppression of eddy activity near the winter solstices (Figure 9b). Additional power over the north polar cap is seen in northern fall and winter. During the dust forcing period, the power in the weather transient group in the winter hemisphere decreases in the 75°S–45°S run but increases in the 45°N–75°N run. Furthermore, the latitudinal region of enhanced eddy activity in the 45°N–75°N run extends from the northern high latitudes to near 20°N, which could facilitate further dust lifting in flushing dust storms.

The tidal group has the largest power among the three groups. In the control run (Figure 9c), there is a maximum in eddy power in the southern subtropics during $L_S = 210°$–$330°$, with secondary maxima in the tropics during $L_S = 60°$–$150°$ and in the northern subtropics in Quartober and Sixtober. Figures 9g and 9k show that, during $L_S = 200°$–$230°$ when dust forcing is imposed, there is an increase in tidal eddy power in the subtropics of the forcing hemisphere. Large increases in the tidal U^* also occur for the other Quartober runs where dust forcing is prescribed at lower latitudes (not shown), which could initiate dust storms.

Observations show that a large dust storm episode is sometimes closely followed in time by a smaller one (e.g., $L_S = 320°$–$336°$ of MY 33, see animation in supporting material) where the latter originates in the northern low latitudes (e.g., Chryse) and travels southward across the equator. The follow-up episode does not appear to be associated with any frontal dust storms as the classical flushing dust storms do though the same general trajectory is followed. This second type of flushing event is most likely due to enhanced tidal eddies.

The $[U_m^*]$ shows a pattern of evolution (Figures 9d, 9h, and 9l) similar to that of the tidal eddy group (Figures 9c, 9g, and 9k), except that there are prominent local maxima at the northern high latitudes in Quartober and Sixtober (Figure 9d). The Quartober high latitude maximum becomes smaller and weaker in the 75°S–45°S run

10.1029/2023JE007956

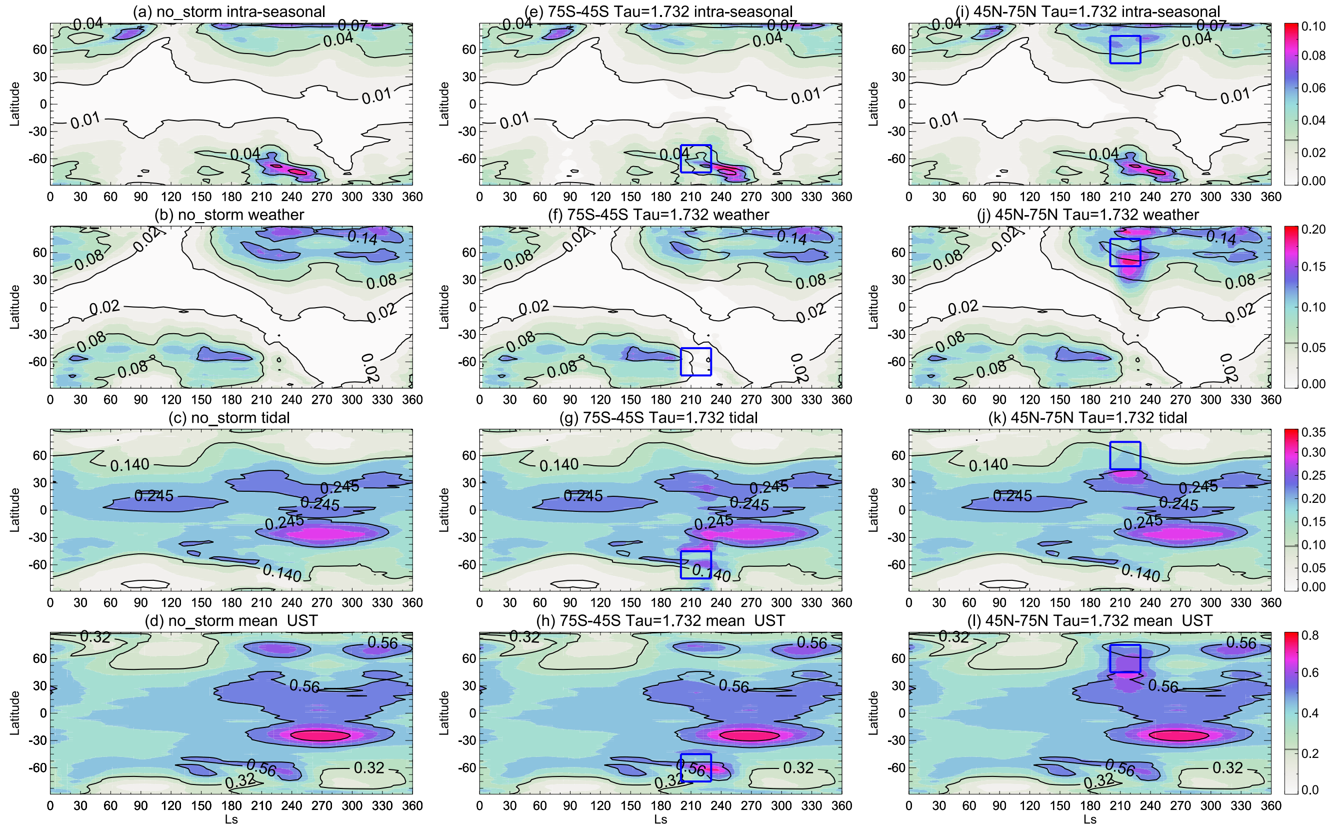

Figure 9. Surface friction velocity (U^*) results (color filled contours) as a function of latitude and L_s for the (a–d) no storm run, (e–h) 75°S–45°S Quartober run, and (i–l) 45°N–75°N Quartober run. The bottom row shows the zonal mean of the 60-sol mean U^* (m/s). Other rows show the square root of the zonal mean scale averaged wavelet power (m/s) (Torrence & Compo, 1998) for the (a, e, i) $P \geq 12$ sols, (b, f, j) $1.7 \leq P < 12$ sols, and (c, g, k) $P < 1.7$ sol eddies. Note that the color bars are different for each row. To facilitate comparison, the no-storm run results are overplotted in black contours in each panel. Blue boxes in (e–l) indicate the time intervals and latitudes of imposed dust.

(Figure 9h). In contrast, it becomes stronger, shifts southward, and connects with the secondary maximum in the subtropics in the 45°N–75°N run (Figure 9l). The latitudes with enhanced $[U_m^*]$ overlap with those with enhanced weather and tidal groups. This suggests that dust in the northern high latitudes could facilitate the development of southward flushing events through the combination of the mean flow, tidal, and weather transient eddies.

4.3. Sixtober Results

The Sixtober runs use the same no-storm baseline but have additional dust added during $L_S = 300°–330°$, again within 30°-wide latitudinal bands centered at several latitudes between 75°S and 75°N. While the optical depths added are the same as those in the Quartober runs, the total optical depths are overall smaller in Sixtober due to the smaller baseline optical depth values (Figure S1 in Supporting Information S1). Other differences with respect to Quartober are that the Sixtober northern polar cap is much larger in extent (Figure 7), and that the Sixtober dust forcing seasonal dates (with a median at $L_S = 315°$) are closer to the northern winter solstice ($L_S = 270°$) but farther from Mars' perihelion ($L_S = 251°$).

Figures 6f–6j shows the $\sqrt{\langle \mathrm{EKE} \rangle}$ time series for the three eddy groups from the Sixtober runs. Similar to the Quartober runs, the intra-seasonal ⟨EKE⟩ is strengthened near the beginning and end of the dust forcing period, the tidal ⟨EKE⟩ increases the most when dust is prescribed at low latitudes, and the weather transient ⟨EKE⟩ is increasingly suppressed as dust forcing moves from the tropics toward the southern high latitudes.

However, some differences between the Quartober and Sixtober results are noticeable. The intra-seasonal ⟨EKE⟩ in the Sixtober 75°S–45°S run increases well above the weather transient ⟨EKE⟩ near $L_S = 300°$, such that it approaches the tidal ⟨EKE⟩ of the control run. This is consistent with the wide-spread latitudinal increase of

10.1029/2023JE007956

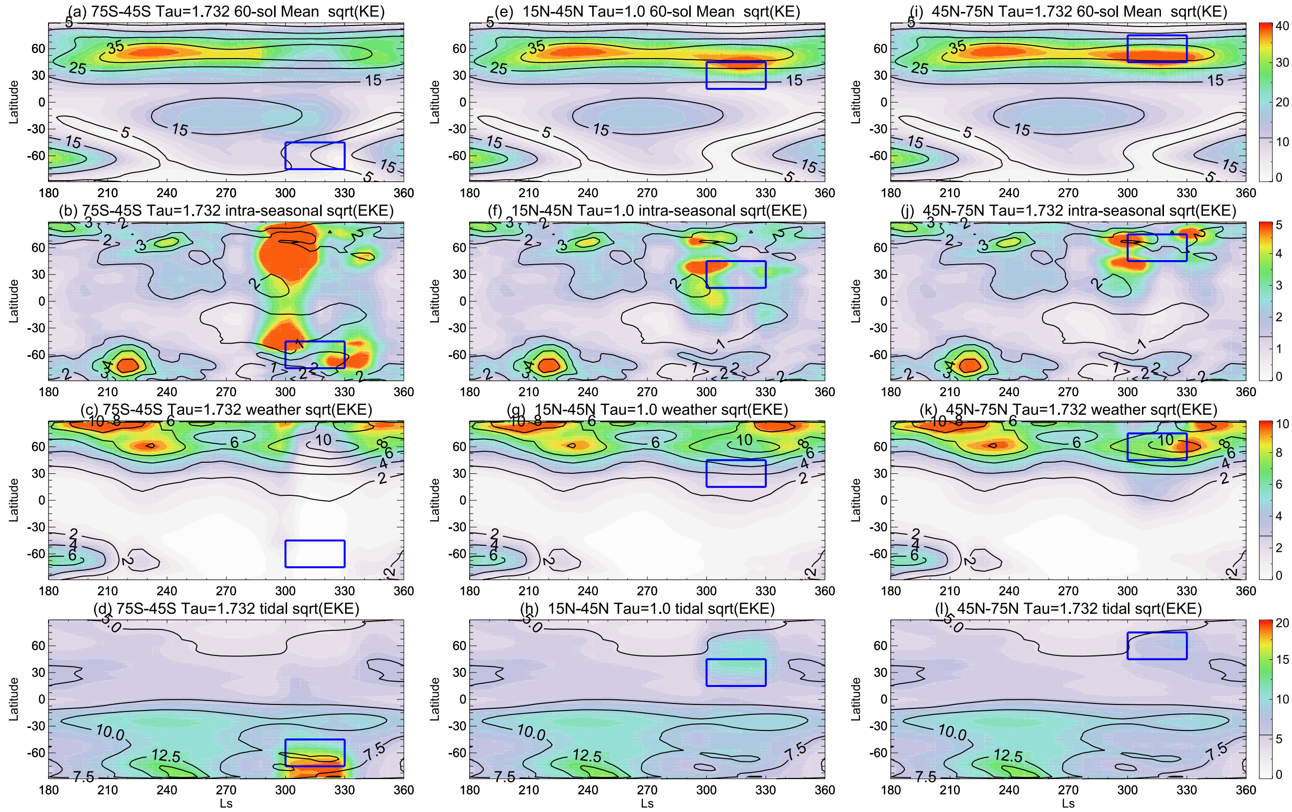

Figure 10. Same as Figure 7, but for Sixtober (left) 75°S–45°S, (middle) 15°N–45°N, and (right) 45°N–75°N runs, and without an indicator of the polar cap edge.

$\sqrt{[\overline{\mathrm{EKE}}]}$ for these eddies (Figure 10b). Accompanying this change, tidal eddies are amplified in the southern mid-high latitudes (Figure 10d), and the northern high latitude maxima for both the mean flow and the weather transient eddies are eliminated (Figures 10a and 10c). For all the other Sixtober and Quartober runs, the intra-seasonal ⟨EKE⟩ does not significantly exceed the weather transient ⟨EKE⟩ (Figure 6).

The weather transient ⟨EKE⟩ in the Sixtober 15°N–45°N run is weaker than that of the control run during the dust forcing period (Figure 6g), but in the Quartober 15°N–45°N run, it is of comparable magnitude (Figure 6b). Figures 10e–10h show that the mean flow maximum in Sixtober is pushed south of its position in the control run, and the weather transient $\sqrt{[\overline{\mathrm{EKE}}]}$ no longer has a local maximum around the north polar cap edge, though the intra-seasonal and tidal eddies increase in the northern hemisphere.

The weather transient ⟨EKE⟩ in the Sixtober 45°N–75°N run is similar to that in the control run (Figure 6f), but in the Quartober 45°N–75°N run, it is larger during the dust forcing period (Figure 6a). These results suggest that high northern latitude dust forcing in Sixtober is not as effective at promoting frontal/flushing dust storms as the imposition of dust forcing in Quartober. This may be a factor in explaining why the observed dust storm episodes are generally less frequent in Sixtober than in Quartober (Wang, Saidel, et al., 2023).

The U^* results for selected Sixtober runs are shown in Figure 11. In comparison with the control run, during L_S = 300°–330°, the power in the tidal group shows enhancement in the vicinity of the latitudes of dust forcing (Figures 11c, 11g, and 11k). The northern hemisphere high latitude maximum in $[U_m^*]$ is removed in the 75°S–45°S run and greatly reduced in the 15°N–45°N run (Figures 11d and 11h). These decreases are also seen in the same region for the eddy power in the weather transient group (Figures 11b and 11f). For the 45°N–75°N run, the northern high latitude $[U_m^*]$ is suppressed, but the northern mid-latitude $[U_m^*]$ increases somewhat (Figure 11l). Furthermore, the region of large power in the weather transient group in the northern hemisphere extends further south in this run (Figure 11j). The combination of the effects in the Sixtober 45°N–75°N run still appears to favor positive feedback on wind stress dust lifting and flushing dust storm development (Figures 11j–11l), though it is

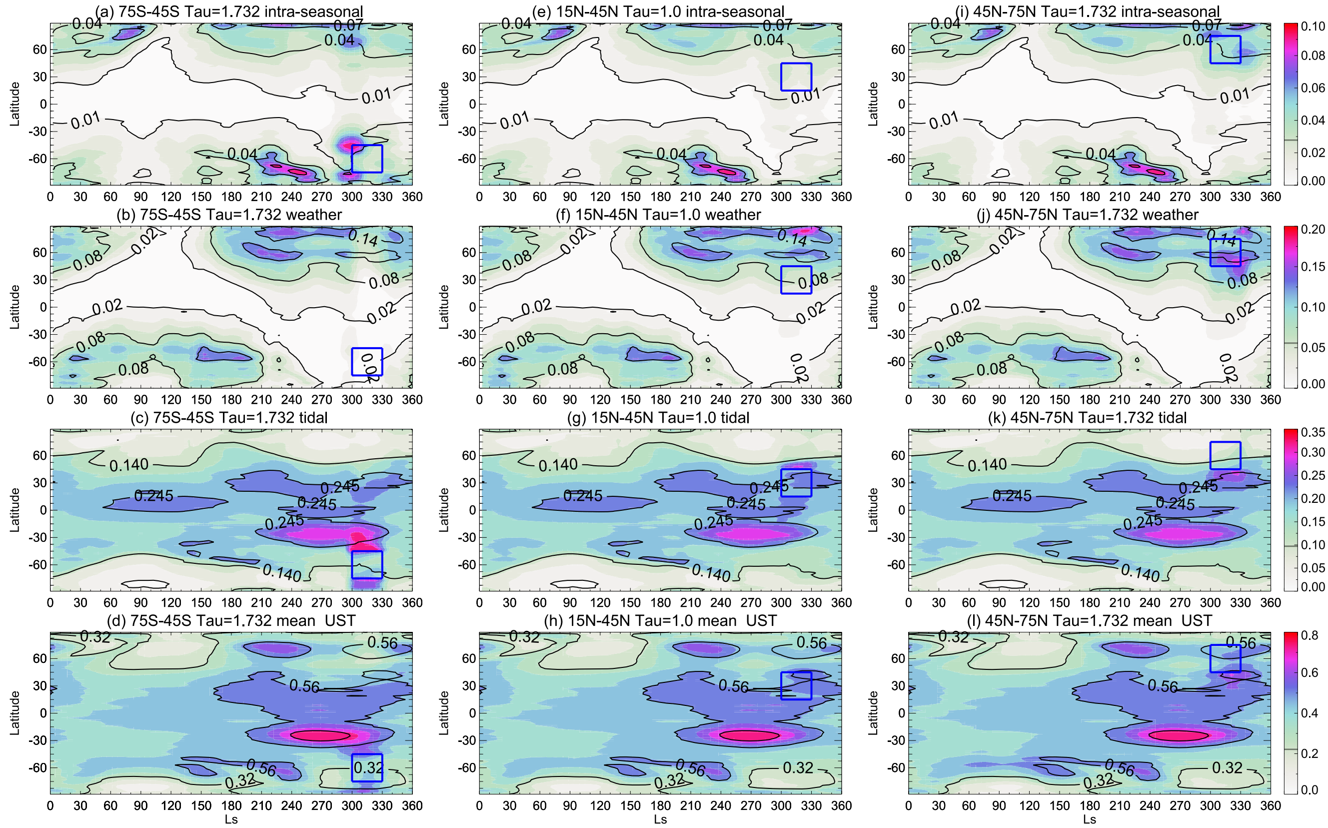

Figure 11. Same as Figure 9, but for Sixtober (a–d) 75°S–45°S run, (e–h) 15°N–45°N run, and (i–l) 45°N–75°N run. Black contours show the results from the no-storm control run. Blue boxes indicate the time intervals and latitudes of imposed dust.

not as strong as in the Quartober 45°N–75°N run (Figures 9j–9l). The feedback is also more limited to the northern high latitudes in Sixtober, where unlike the Quartober cases, the positive feedback in Sixtober ceases when dust forcing is shifted even to 15°N–45°N (Figures 11e–11h).

5. Summary and Discussion

In this paper, we employed idealized, large-scale dust radiative forcing within the MarsWRF model to examine how Martian circulation components respond from a global perspective. Dust was prescribed in a longitudinally uniform way across several latitudinal bands. While this behavior mimics only a subset of observed regional dust storms, it represents only our first examination of a set of experiments in a planned series that will investigate a range (in extent, location, timing, etc.) of dust storm forcing scenarios. We seek to identify potential positive and negative feedback mechanisms that might help explain the growth and decay cycles of large dust storm episodes. Previous theories of dust storm development mechanisms involved the interactions of different circulation components (Battalio & Wang, 2020; Martinez-Alvarado et al., 2009), such as the "tidal gate" theory of flushing storms (Wang et al., 2003). This study focuses mostly on the response of eddy groups distinguished by their characteristic time scales to the imposition of large-scale dust storm-like radiative forcing in the MarsWRF model.

We specifically examined the response of the simulated atmosphere in terms of the (60 sols) time mean flow and eddies with tidal ($P < 1.7$ sols), "weather" ($1.7 \leq P < 12$ sols), and intra-seasonal ($P \geq 12$ sols) periodicities. The simulations were motivated by spacecraft observations that show that dust storm episodes typically evolve through different stages at different latitudes and occur most often in Quartober and Sixtober (in northern fall and winter, and away from the solstice) (Battalio & Wang, 2021; Kass et al., 2016). Wavelet analysis was employed to decompose transient eddies into the three eddy groups. To account for the chaotic nature of the dynamical system, especially for the weather transients, statistical analysis over multiple simulation years using the same repeating forcing was performed.

The results suggest that in Quartober, enhanced dust in the northern high latitudes leads to increased baroclinicity near the surface and hence enhanced "weather" transient eddy activity. While it is still uncertain whether the dust within northern Quartober episodes is primarily lifted by baroclinic fronts or simply concentrated along them, stronger frontal cyclones would seem likely to be associated with dustier and larger frontal dust storm instances (Hollingsworth & Kahre, 2010; Wang et al., 2003). If this is the case, then dust lifting associated with frontal storm instances at these latitudes would tend to act as positive feedback on itself, that is, more dust leads to stronger "weather" eddies, which in turn leads to dustier and larger frontal dust storm instances, at least when the dust storm instances remain within the northern "storm zones" (Hollingsworth et al., 1996).

Large frontal storm instances naturally develop an equatorward extension within northern low topography regions because of the storm size and storm zone location. However, the occurrence of significant flushing indicates that the storms move out of the northern mid-latitudes into the low latitudes where baroclinic cyclogenesis no longer operates efficiently. Such transference appears to be associated with the interaction between frontal cyclones and thermal tides (Wang et al., 2003). Interestingly, as dust radiative heating increases in the northern subtropics and tropics, the simulated tidal component of the transient eddy activity also increases. This indicates that as large frontal systems extend equatorward toward the topics, the radiative heating of the dust will increase the circulation associated with the thermal tides, and hence (with favorable phasing of the tides and the cyclone development) again cause positive feedback that will increase the chance and intensity of southward propagating regional storm episodes.

Once dust is advected far into the southern hemisphere, the model results suggest that the feedback of dust heating on further intensification of northern frontal/flushing dust storm becomes negative. This is because the elevated dust optical depths in the southern hemisphere augment the zonal mean overturning circulation such that the near surface baroclinicity in the opposing winter hemisphere is reduced. Furthermore, with dust opacity elevated in the southern summer mid-latitudes rather than the tropics, the globally averaged eddy kinetic energy of the tidal group is closer to that in the "no-storm" control run. These effects result in a reduced likelihood of new dust lifting associated with the weather group in the northern high latitudes and reduced lower latitude dust lifting associated with the tidal group. This may be a potential long-range mechanism of storm sequence termination, with the caveat that the storm sequences do not become a global dust storm episode. If the enhanced zonal mean circulation can vertically and horizontally advect sufficient dust, then a transition to a global dust storm may occur, where a strongly enhanced zonal mean circulation coupled with dramatically altered thermal tides (Guzewich et al., 2014) redistributes dust and activates additional dust lifting centers elsewhere, for example, the Solis/Syria region during the 2001 and 2007 global storm (Martinez-Alvarado et al., 2009; Strausberg et al., 2005). Future simulations using radiatively and dynamically interactive dust transport may shed light on the transition to a global dust storm.

The different types of positive and negative feedbacks suggested by the simulations may provide insight into the cascading nature of storm growth, where small differences in storm extent or optical thickness may allow it to cross thresholds that activate new dynamical pathways, as suggested by Toigo et al. (2018). For example, whether dust forcing generated by cyclonic frontal dust storms extends sufficiently into the latitudes that excite a significant tidal response may be important for facilitating the "tidal gate" mechanism that potentially determines whether the storm flushes to low latitudes; for a storm that has been transported across the tropics and into the southern mid-latitudes, its size and optical thickness may be important in determining whether an enhanced zonal mean circulation reduces winter hemisphere baroclinicity, suppressing further cyclonic frontal storm initiation and flushing storm growth, or alternatively spreads dust globally and further enhances the zonal mean circulation and modifies the thermal tides, activating additional dust lifting centers. Each threshold marks a transition into a new regime and hence seems likely to be a part of a growth cascade that starts with small-scale local dust lifting and in some rare cases ends in a global dust storm.

While the Sixtober and Quartober sextons are both associated with interhemispheric flushing dust storms in general, there are subtle differences. Specifically, during Sixtober, northern high latitude dust does not encourage frontal/flushing dust storms as strongly as it does in Quartober. The result may help explain the different characteristics between the observed Quartober and Sixtober large dust storm episodes, where the Sixtober episodes tend to have fewer and smaller northern flushing dust storm sequences (Wang, Saidel, et al., 2023).

Data Availability Statement

The archive for simulations used in this paper can be found at Zenodo (Wang, Toigo, & Richardson, 2023). The Mars Daily Global Maps (MDGMs) are available at Harvard Dataverse (Wang et al., 2020). The OpenMars database can be downloaded from the Open University (Holmes et al., 2019). The EMARS data set is available at the Penn State Data Commons (Greybush et al., 2018).

Acknowledgments

Modeling and analysis in this study were supported by NASA Grants 80NSSC21K1831 and 80NSSC20K0469. Resources supporting simulations for this paper were provided by the NASA High-End Computing (HEC) program through the NASA Advanced Supercomputing (NAS) division at the Ames Research Center. Mars Daily Global Maps were supported by NASA Grant 80NSSC20K1056 and were made using the Smithsonian High Performance Cluster (SI/HPC), Smithsonian Institution (https://doi.org/10.25572/SIHPC). We thank R. J. Wilson and an anonymous reviewer for their reviews.

References

Banfield, D., Conrath, B., Pearl, J. C., Smith, M. D., & Christensen, P. (2000). Thermal tides and stationary waves on Mars as revealed by Mars Global Surveyor thermal emission spectrometer. *Journal of Geophysical Research*, *105*(E4), 9521–9537. https://doi.org/10.1029/1999je001161

Banfield, D., Conrath, B. J., Gierasch, P. J., Wilson, R. J., & Smith, M. D. (2004). Traveling waves in the Martian atmosphere from MGS TES Nadir data. *Icarus*, *170*(2), 365–403. https://doi.org/10.1016/j.icarus.2004.03.015

Banfield, D., Spiga, A., Newman, C., Forget, F., Lemmon, M., Lorenz, R., et al. (2020). The atmosphere of Mars as observed by Insight. *Nature Geoscience*, *13*(3), 190–198. https://doi.org/10.1038/s41561-020-0534-0

Barnes, J. R. (1980). Time spectral-analysis of mid-latitude disturbances in the martian atmosphere. *Journal of Geophysical Research*, *37*(9), 2002–2015. https://doi.org/10.1175/1520-0469(1980)037<2002:tsaomd>2.0.co;2

Battalio, J. M. (2022). Transient eddy energetics on Mars in three reanalysis datasets. *Journal of the Atmospheric Sciences*, *79*(2), 361–382. https://doi.org/10.1175/JAS-D-21-0038.1

Battalio, J. M., Martinez, G., Newman, C., de la Torre Juarez, M., Sanchez-Lavega, A., & Viudez-Moreiras, D. (2022). Planetary waves traveling between Mars Science Laboratory and Mars 2020. *Geophysical Research Letters*, *49*(21), e2022GL100866. https://doi.org/10.1029/2022GL100866

Battalio, J. M., & Wang, H. (2021). The Mars dust activity database (MDAD): A comprehensive statistical study of dust storm sequences. *Icarus*, *354*, 114059. https://doi.org/10.1016/j.icarus.2020.114059

Battalio, M. J., & Wang, H. (2020). Eddy evolution during large dust storms. *Icarus*, *338*, 113507. https://doi.org/10.1016/j.icarus.2019.113507

Cantor, B. A. (2007). MOC observations of the 2001 Mars planet-encircling dust storm. *Icarus*, *186*(1), 60–96. https://doi.org/10.1016/j.icarus.2006.08.019

Giuranna, M., Wolkenberg, P., Grassi, D., Aronica, A., Aoki, S., Scaccabarozzi, D., et al. (2021). The current weather and climate of Mars: 12 years of atmospheric monitoring by the planetary Fourier spectrometer on Mars express. *Icarus*, *353*, 113406. https://doi.org/10.1016/j.icarus.2019.113406

Greybush, S. J., Gillespie, H. E., & Wilson, R. J. (2019). Transient eddies in the TES/MCS ensemble Mars atmosphere reanalysis system (EMARS). *Icarus*, *317*, 158–181. https://doi.org/10.1016/j.icarus.2018.07.001

Greybush, S. J., Kalnay, E., Hoffman, M. J., & Wilson, R. J. (2013). Identifying Martian atmospheric instabilities and their physical origins using bred vectors. *Quarterly Journal of the Royal Meteorological Society*, *139*(672), 639–653. https://doi.org/10.1002/qj.1990

Greybush, S. J., Kalnay, E., Wilson, R. J., Hoffman, R. N., Nehrkorn, T., Leidner, M., et al. (2018). The ensemble Mars atmosphere reanalysis system (EMARS) version 1.0 dataset [Dataset]. Geoscience Data Journal, *6*(2), 137–150. https://doi.org/10.18113/D3W375

Greybush, S. J., Kalnay, E., Wilson, R. J., Hoffman, R. N., Nehrkorn, T., Leidner, M., et al. (2019). The ensemble Mars atmosphere reanalysis system (EMARS) version 1.0. *Geoscience Data Journal*, *6*(2), 137–150. https://doi.org/10.1002/gdj3.77

Guzewich, S. D., Wilson, R. J., McConnochie, T. H., Toigo, A. D., Banfield, D. J., & Smith, M. D. (2014). Thermal tides during the 2001 Martian global-scale dust storm. *Journal of Geophysical Research*, *119*(3), 506–519. https://doi.org/10.1002/2013JE004502

Harri, A. M., Genzer, M., Kemppinen, O., Kahanpaa, H., Gomez-Elvira, J., Rodriguez-Manfredi, J. A., et al. (2014). Pressure observations by the Curiosity rover: Initial results. *Journal of Geophysical Research: Planets*, *119*(1), 82–92. https://doi.org/10.1002/2013JE004423

Hinson, D. P., Wang, H., & Smith, M. D. (2012). A multi-year survey of dynamics near the surface in the northern hemisphere of Mars: Short-period baroclinic waves and dust storms. *Icarus*, *219*(1), 307–320. https://doi.org/10.1016/j.icarus.2012.03.001

Hinson, D. P., & Wilson, R. J. (2021). Baroclinic waves in the northern hemisphere of Mars as observed by the MRO Mars climate sounder and the MGS thermal emission spectrometer. *Icarus*, *357*, 114152. https://doi.org/10.1016/j.icarus.2020.114152

Hollingsworth, J. L., Haberle, R. M., Barnes, J. R., Bridgers, A. F. C., Pollack, J. B., Lee, H., & Schaeffer, J. (1996). Orography control of storm zones on Mars, Nature. *Nature*, *380*(6573), 413–416. https://doi.org/10.1038/380413a0

Hollingsworth, J. L., & Kahre, M. A. (2010). Extratropical cyclones, frontal waves, and Mars dust: Modeling and considerations. *Geophysical Research Letters*, *37*(22), L22202. https://doi.org/10.1029/2010GL044262

Holmes, J., Lewis, S., & Patel, M. (2019). OpenMARS database [Dataset]. The Open University Collection. https://doi.org/10.21954/ou.rd.c.4278950

Holmes, J. A., Lewis, S. R., & Patel, M. R. (2020). OpenMARS: A global record of Martian weather from 1999–2015. *Planetary and Space Science*, *188*, 104962. https://doi.org/10.1016/j.pss.2020.104962

Kahre, M. A., Murphy, J. R., Newman, C. E., Wilson, R. J., Cantor, B. A., Lemmon, M. T., & Wolff, M. J. (2017). The Mars dust cycle. In R. M. Haberle, R. T. Clancy, F. Forget, M. D. Smith, & R. W. Zurek (Eds.), *Atmosphere and climate of Mars* (pp. 295–337).

Kass, D. M., Kleinböhl, A., McCleese, D. J., Schofield, J. T., & Smith, M. D. (2016). Interannual similarity in the Martian atmosphere during the dust storm season. *Geophysical Research Letters*, *43*(12), 6111–6118. https://doi.org/10.1002/2016GL068978

Kleinböehl, A., Wilson, R. J., Kass, D., Schofield, J. T., & McCleese, D. J. (2013). The semidiurnal tide in the middle atmosphere of Mars. *Geophysical Research Letters*, *40*(10), 1952–1959. https://doi.org/10.1002/grl.50497

Lee, C., Richardson, M. I., Newman, C. E., & Mischna, M. A. (2018). The sensitivity of solsticial pauses to atmospheric ice and dust in the MarsWRF general circulation model. *Icarus*, *311*, 23–34. https://doi.org/10.1016/j.Icarus.2018.03.019

Lewis, S. R., & Barker, P. R. (2005). Atmospheric tides in a Mars general circulation model with data assimilation. Planetary atmospheres, ionospheres, and magnetospheres. *Advances in Space Research*, *36*(11), 2162–2168. https://doi.org/10.1016/j.asr.2005.05.122

Lewis, S. R., Collins, M., Read, P. L., Forget, F., Hourdin, F., Fournier, R., et al. (1999). A climate database for Mars. *Journal of Geophysical Research*, *104*(E10), 24177–24194. https://doi.org/10.1029/1999JE001024

Lewis, S. R., Mulholland, D. P., Read, P. L., Montabone, L., Wilson, R. J., & Smith, M. D. (2016). The solsticial pause on Mars: 1. A planetary wave reanalysis. *Icarus*, *264*, 456–464. https://doi.org/10.1016/j.icarus.2015.08.039

Martin, J. J., & Zurek, R. W. (1993). An analysis of the history of dust activity on Mars. *Journal of Geophysical Research*, *98*(E2), 3221–3246. https://doi.org/10.1029/92JE02937

Martinez-Alvarado, O., Montabone, L., Lewis, S. R., Moroz, I. M., & Read, P. L. (2009). Transient teleconnection event at the onset of a planet-encircling dust storm on Mars. *Annales Geophysicae*, *27*(9), 3663–3676. https://doi.org/10.5194/angeo-27-3663-2009

Mischna, M. A., Lee, C., & Richardson, M. I. (2012). Development of a fast, accurate radiative transfer model for the Martian atmosphere, past and present. *Journal of Geophysical Research: Planets*, *117*(E10), E10009. https://doi.org/10.1029/2012JE004110

Montabone, L., Forget, F., Millour, E., Wilson, R. J., Lewis, S. R., Cantor, B., et al. (2015). Eight-year climatology of dust optical depth on Mars. *Icarus*, *251*, 65–95. https://doi.org/10.1016/j.icarus.2014.12.034

Montabone, L., Spiga, A., Kass, D. M., Kleinbohl, A., Forget, F., & Millour, E. (2020). Martian year 34 column dust climatology from Mars Climate Sounder observations: Reconstructed maps and model simulations. *Journal of Geophysical Research: Planets*, *125*(8), e2019JE006111. https://doi.org/10.1029/2019JE006111

Mulholland, D. P., Lewis, S. R., Read, P. L., Madeleine, J., & Forget, F. (2016). The solsticial pause on Mars: 2 modeling and investigation of causes. *Icarus*, *264*, 465–477. https://doi.org/10.1016/j.icarus.2015.08.038

Newman, C. E., Lee, C., Mischna, M. A., Richardson, M. I., & Shirley, J. H. (2019). An initial assessment of the impact of postulated orbit-spin coupling on Mars dust storm variability in fully interactive dust simulations. *Icarus*, *317*, 649–668. https://doi.org/10.1016/j.icarus.2018.07.023

Newman, C. E., Read, P. L., & Lewis, S. R. (2004). Investigating atmospheric predictability on Mars using breeding vector in a general-circulation model. *Quarterly Journal of the Royal Meteorological Society*, *130*(603), 2971–2989. https://doi.org/10.1256/qj.03.209

Newman, C. E., & Richardson, M. I. (2015). The impact of surface dust source exhaustion on the Martian dust cycle, dust storms and interannual variability, as simulated by the MarsWRF General Circulation Model. *Icarus*, *257*, 47–87. https://doi.org/10.1016/j.icarus.2015.03.030

Powers, J. G., Klemp, J. B., Skamarock, W. C., Davis, C. A., Dudhia, J., Gill, D. O., et al. (2017). The Weather Research and Forecasting Model overview, system efforts, and future directions. *Bulletin of the American Meteorological Society*, *98*(8), 1717–1737. https://doi.org/10.1175/BAMS-D-15-00308.1

Richardson, M. I., Toigo, A. D., & Newman, C. E. (2007). PlanetWRF: A general purpose, local to global numerical model for planetary atmospheric and climate dynamics. *Journal of Geophysical Research*, *112*(E9), E09001. https://doi.org/10.1029/2006JE002825

Sheng, J., & Derome, J. (1991). An observational study of the energy transfer between the seasonal mean flow and transient eddies. *Tellus A: Dynamic Meteorology and Oceanography*, *43*(2), 128–144. https://doi.org/10.3402/tellusa.v43i2.11921

Smith, M. D. (2008). Spacecraft observations of the Martian atmosphere. *Annual Review of Earth and Planetary Sciences*, *36*(1), 191–219. https://doi.org/10.1146/annurev.earth.36.031207.124334

Smith, M. D. (2019). Local time variation of water ice clouds on Mars as observed by THEMIS. *Icarus*, *333*, 273–282. https://doi.org/10.1016/j.icarus.2019.06.009

Strausberg, M. J., Wang, H., Richardson, M. I., Ewald, S. P., & Toigo, A. D. (2005). Observations of the initiation and evolution of the 2001 Mars global dust storm. *Journal of Geophysical Research*, *110*(E2), E02006. https://doi.org/10.1029/2004JE002361

Streeter, P. M., Lewis, S. R., Patel, M. R., Holmes, J. A., Fedorova, A. A., Kass, D. M., & Kleinbohl, A. (2021). Asymmetric impacts on Mars' polar vortices from an equatorial global dust storm. *Journal of Geophysical Research*, *126*, 5. https://doi.org/10.1029/2020JE006774

Toigo, A. D., Lee, C., Newman, C. E., & Richardson, M. I. (2012). The impact of resolution on the dynamics of the Martian global atmosphere: Varying resolution studies with the MarsWRF GCM. *Icarus*, *221*(1), 276–288. https://doi.org/10.1016/j.icarus.2012.07.020

Toigo, A. D., Richardson, M. I., Wang, H., Guzewich, S. D., & Newman, C. E. (2018). The cascade from local to global dust storms on Mars: Temporal and spatial thresholds on thermal and dynamical feedback. *Icarus*, *302*, 514–536. https://doi.org/10.1016/j.icarus.2017.11.032

Toigo, A. D., & Waugh, D. W. (2022). Connections between the transient polar warming and solstitial pause on Mars. *The Planetary Science Journal*, *3*(9), 208. https://doi.org/10.3847/PSJ/ac8550

Torrence, C., & Compo, G. P. (1998). A practical guide to wavelet analysis. *Bulletin of the American Meteorological Society*, *79*(1), 61–78. https://doi.org/10.1175/1520-0477(1998)079<0061:APGTWA>2.0.CO;2

Wang, H. (2017). Major dust storm and westward traveling waves on Mars. *Geophysical Research Letters*, *44*(8), 3493–3501. https://doi.org/10.1002/2017GL072894

Wang, H., Battalio, M., & Huber, Z. (2020). Replication data for: MRO MARCI Mars daily global maps V2 [Dataset]. Harvard Dataverse, V4. https://doi.org/10.7910/DVN/U3766S

Wang, H., & Richardson, M. I. (2015). The origin, evolution, and trajectory of large dust storms on Mars during Mars years 24–30 (1999–2011). *Icarus*, *251*, 112–127. https://doi.org/10.1016/j.icarus.2013.10.033

Wang, H., Richardson, M. I., Wilson, R. J., Ingersoll, A. P., & Zurek, R. W. (2003). Cyclones, tides, and the origin of major dust storms on Mars. *Geophysical Research Letters*, *30*(9), 1488. https://doi.org/10.1029/2002GL016828

Wang, H., Saidel, M., Richardson, M. I., Toigo, A. D., & Battalio, J. M. (2023). Martian dust storm distribution and annual cycle from Mars daily global map observations. *Icarus*, *394*, 115416. https://doi.org/10.1016/j.icarus.2022.115416

Wang, H., Toigo, A. D., & Richardson, M. I. (2023). MarsWRF imposed dust simulations for investigation of dust storm trajectories (1.0) [Dataset]. Zenodo. https://doi.org/10.5281/zenodo.8000291

Wang, H., Zurek, R. W., & Richardson, M. I. (2005). Relationship between frontal dust storm and transient eddy activity in the northern hemisphere of Mars as observed by Mars Global Surveyor. *Journal of Geophysical Research*, *110*, E7. https://doi.org/10.1029/2005JE002423

Wilson, R. J. (2012a). Martian dust storms, thermal tides and the Hadley circulation. In *Abstract 8069, comparative climatology of terrestrial planets, Boulder, CO, June 2012*. Retrieved from http://www.lpi.usra.edu/meetings/climatology2012/pdf/8069.pdf

Wilson, R. J. (2012b). The role of thermal tides in the Martian dust cycle. In *European planetary science congress, Madrid, Spain, September, 2012*. Retrieved from http://meetingorganizer.copernicus.org/EPSC2012/EPSC2012-798-1.pdf

Wilson, R. J., & Hamilton, K. (1996). Comprehensive model simulation of thermal tides in the Martian atmosphere. *Journal of the Atmospheric Sciences*, *53*(9), 1290–1326. https://doi.org/10.1175/1520-0469(1996)053<1290:cmsott>2.0.co;2

Wilson, R. J., Lewis, S. R., & Montabone, L. (2007). Thermal tides in an assimilation of three years of TES data from Mars Global Surveyor. In *Abstract 3307, seventh international Mars conference, July, 2007*. Retrieved from http://www.lpi.usra.edu/meetings/7thmars2007/pdf/3307.pdf

Zurek, R. W., & Leovy, C. B. (1981). Thermal tides in the dusty Martian atmosphere: A verification of theory. *Science*, *213*(4506), 437–439. https://doi.org/10.1126/science.213.4506.437